Science Requirements Document

Version 2.1

1 April 2010

for

Experimental and Computational Study of Coflow Laminar Diffusion Flames in a Microgravity Environment

Principal Investigator:

Marshall B. Long

Yale University

New Haven, CT 06520-8284

Co-Investigator:

Mitchell D. Smooke

Yale University

New Haven, CT 06520-8284

Project Scientist:

Dennis Stocker, NASA GRC

EXECUTIVE SUMMARY

The proposed work will build upon our ground-based microgravity studies in which advanced adaptive (parallel) computational algorithms and multidimensional imaging techniques were performed to characterize buoyant and nonbuoyant diffusion flames. The computational work has facilitated the development of detailed soot models while the experimental work performed has built expertise in bringing two-dimensional, laboratory-quality diagnostics to a microgravity environment. The experimental results of our previous microgravity combustion studies have provided the most rigorous testing of our combustion models to date. Experiments were performed on the KC-135 of a nitrogen-diluted methane coflow laminar diffusion flame to measure flame chemiluminescence, temperature, major species, and soot distributions. The results compared well with computations in the moderately dilute cases, but discrepancies were revealed in the case of the more dilute flames, particularly with the observed lift-off heights and extinction limits. Additionally, the weak flames and the sooting flames were observed to be sensitive to the presence of g-jitter, making clear analysis difficult. It is at these extremes of the fuel dilution spectrum that the most interesting effects can be observed. Further, by extending the studies over a broad range of conditions, discrepancies between measurement and computation have been discovered that previous laboratory studies of this flame failed to reveal.

We propose to concentrate this study on flame phenomena at the extremes of the fuel dilution spectrum – namely dilute flames near extinction and highly-sooting pure-fuel flames. Previous work has shown that both weak flames and highly sooting flames require long periods of "clean" microgravity to reach a steady state. The conditions aboard the International Space Station (ISS) will be ideal in this regard. The intended flight experiments will provide insights into flame stability, extinction, and soot processes that are unavailable in ground-based microgravity facilities.

Our project goals include the generation of improved computational models with improved soot submodels that are effective for both dilute flames and sooting flames that vary from low to high soot loading levels. The enhanced time and spatial scales in a microgravity environment will be important for achieving both goals. Experimentally, we plan to study methane and ethylene diffusion flames over a wide range of test conditions. For the more dilute flames, measurements will be made of flame chemiluminesence of *OH** and CH* to observe variations in lift-off height and flame shape as extinction limits are approached. The sooting tendencies of

the more fuel-rich flames will be investigated using soot luminosity and laser extinction measurements to determine soot temperatures and soot volume fractions. Flame temperatures in nonsooting regions will be measured using thin-filament pyrometry. Based on observations, modifications can be made to the kinetics and soot model to match better the experimental results. If the overall agreement of the measurements and computations is good, the results of the computations can be “mined” to provide insight on species (and hence chemical processes) that cannot be measured directly using the diagnostics available for the proposed experiment.

TABLE OF CONTENTS

1 INTRODUCTION

1.1 Background and Overview

Diffusion flames are the flame type of most practical combustion devices. The ability to predict the coupled effects of complex transport phenomena with detailed chemical kinetics in such systems is critical in the modeling of turbulent reacting flows and in understanding the processes by which soot formation and radiative transfer take place. In addition, an understanding of those factors that affect flame extinction in diffusion flames is critical in the suppression of fires and in improving engine efficiency. While normal gravity combustion studies can provide important information on combustion processes, the effects of gravitational forces often complicate the interpretation of both computational and experimental results. Momentum effects dominate most practical combustion devices, but the contribution of buoyancy forces is hard to eliminate in normal gravity. A goal of the study will be to apply sophisticated numerical tools and quantitative diagnostic techniques to the study of hydrocarbon diffusion flames in a microgravity environment. This will lead to a more detailed understanding of the interaction of convection, diffusion and chemistry under momentum-dominated conditions.

A number of diffusion flame studies have been carried out in a microgravity environment [1-28]. These studies have ranged from methods to evaluate flame structure, to observations of soot processes. The studies indicated that, while computational models based upon parabolic approximations to the governing equations provided adequate comparisons with experimental observations, a better understanding of kinetic effects and axial diffusion in these flames is needed. In addition, only minimal temperature and species composition measurements were made in these systems. Many of the studies that investigated soot processes in nonbuoyant flames focused on the measurement of soot volume fractions and soot structure investigations. Our own study of microgravity laminar coflow diffusion flames, which began in 1996, sought to investigate many of these issues while bringing a combined computational/experimental program to bear on these problems [12, 14, 29, 30]. The results of this program are discussed in the next section.

1.2 Results from Ground-Based Experiments

Our microgravity (μg) combustion experiments proceeded in two phases. The first phase involved extracting reliable, quantitative information from flame chemiluminescence measurements and using this technique in a microgravity flame study aboard the KC-135 reduced-gravity aircraft. After this work increased our experimental expertise and understanding of microgravity diffusion flame behavior, a variety of two-dimensional laser diagnostics were brought to the KC-135 to allow for the measurement of temperature, major species, and soot distributions. These μg measurements afforded the most rigorous set of comparisons with flame computations to date [12, 14, 30-32].

1.3 Burner Configuration

The flame chosen for our initial investigation consisted of nitrogen-diluted methane fuel surrounded by an air coflow. The burner was designed to have well-defined velocity and temperature boundary conditions to facilitate comparisons between computations and experiments. The burner has a central fuel jet (4 mm inner diameter, 0.4 mm wall thickness) surrounded by coflowing air (50 mm inner diameter). The standard flow conditions, which have been measured and modeled extensively in normal gravity, consist of fuel composed of 65% CH_4 diluted with 35% N_2 by volume (denoted 65/35 in later discussions). The plug flow exit velocity of both fuel and coflow was 35 cm/s. These conditions produce a blue flame roughly 3 cm in length with a lift-off height of 5.5 mm in normal gravity. A wide range of fuel dilution levels was measured in this study. The CH_4/N_2 fuel composition varied from 100% CH_4 (denoted 100/0) to 30% CH_4 (denoted 30/70) in 5% increments, with fuel and air exit velocities held fixed at 35 cm/s. For all conditions, the flame was lifted from the burner surface so that the assumption of negligible heat loss to the burner is an excellent one.

1.4 Computational Approach

The computational model used to compute the temperature field, velocities, and species concentrations solves the full set of elliptic two-dimensional governing equations for mass, momentum, species, and energy conservation on a two-dimensional mesh. The resulting nonlinear equations are then solved on an IBM RS/6000 Model 590 computer by a combination of time integration and Newton's method.

Flame structure was calculated over a range of flow conditions in both μg and normal gravity. These computations were performed for CH_4/N_2 mixtures ranging from 30/70 to 75/25. Calculations were not performed at flow conditions less dilute than 75/25 since these flames were observed to produce soot, which was not included in the computational model.

1.5 Flame Emission Tomography

Initial work focused on non-intrusive flame chemiluminescence tomography measurements of excited-state *CH* ($A^2\Delta$, denoted *CH**) and excited-state *OH* ($A^2\Sigma$, denoted *OH**), which are common flame radicals. These measurements were made as quantitative as possible through a thorough investigation of experimental issues, data analysis and interpretation, and evaluation of chemical kinetic models. Although uncertainties in the production reaction rate coefficients for *CH** and *OH** limit our ability to predict quantitatively the optical emission from methane flames to within a factor of six, this diagnostic development work led to some important conclusions. First, we learned that quantitative number densities of *CH** and *OH** could be measured in a short time with a simple, compact optical setup that could be made compatible with existing microgravity facilities. Additionally, the *CH**, *OH**, and ground-state *CH* distributions were seen to be spatially coincident in the flame anchoring region. Therefore, the ground-state *CH* distribution, which is easily computed, and the readily measured *CH**/*OH** distributions can be used to provide a consistent and convenient way of comparing lift-off height and flame shape in the diffusion flames under investigation.

The measurement of flame chemiluminescence requires only a modest experimental setup: an unintensified, cooled CCD camera and an appropriate interference filter, with the lens aperture and burner/lens distance chosen to allow a wide depth of field. Several modifications to the laboratory-based experimental configuration were required to make flame emission measurements aboard the KC-135 reduced-gravity aircraft. The burner and ignition system were housed inside a windowed pressure vessel to maintain standard atmospheric pressure. The combustion vessel and all associated measurement equipment were mounted in a modified drop frame. An external control rack contained a microcomputer to regulate experimental systems and acquire and store quantitative flame emission images. Both equipment racks were bolted to the floor of the aircraft. A laser calibration method can be performed, post-flight, to relate this measured emission signal to an absolute light level.

Appropriate background images, taken for both *CH** and *OH** with the flame extinguished, are subtracted from the raw emission signal. Since the emission measurements are integrated through the collection optics along a line-of-sight, an Abel inversion is then performed to recover the spatially-resolved emission profile. Calibration measurements and a spectral overlap correction can now be applied to quantify the measured intensity level, although spatial information regarding flame shape and lift-off height can be seen with no additional measurement or post-processing.

Flame emission measurements were performed in µg and 1g over a wide range of dilution levels, from 50/50 to 100/0. The base of the flame, where the chemiluminescence signal is strongest, remained extremely stable over the 10 s integration time for all conditions studied. Measured flame shape, as indicated by the spatial distributions of the *CH** and *OH** radicals, can change significantly between normal gravity and microgravity. In general, a microgravity flame is shorter, wider, and has a higher flame front curvature relative to its normal gravity counterpart. Furthermore, since methane is lighter than air, density effects produce a normal gravity flame with a higher lift-off than the corresponding µg flame. These effects can be seen in both computed *CH* profiles and measured *CH** profiles, shown in the 65/35 flame in Fig. 1. Here the structural agreement is excellent for lift-off and flame shape, in both normal and microgravity. Although the computed flame length may appear to be over-predicted at this flow condition, *CH** does not exist at the flame tip and as such is not a good indicator of flame length.

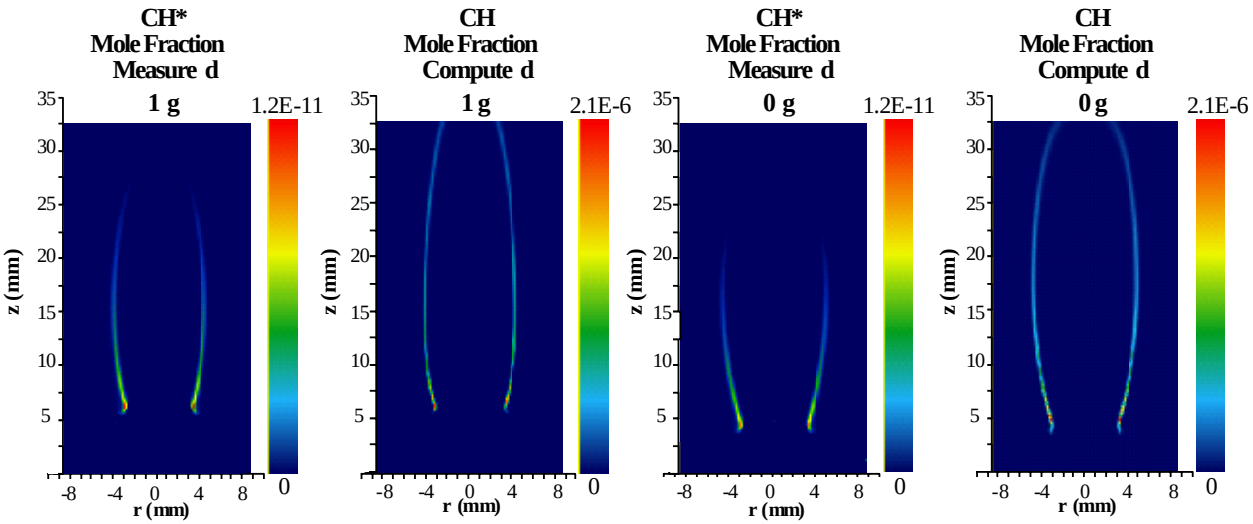

Fig. 1. Measured and computed flame structure at standard flow conditions.

We define the measured lift-off as the height above the burner where the *CH**/*OH** maximum occurs, and similarly for *CH* in the computations. All three peaks occupy the same spatial location, as shown in earlier work. The measured and computed lift-off heights, both in μg and normal gravity, can now be plotted as a function of methane level in the fuel stream as shown in Fig. 2. In addition to the lift-off heights derived from the emission measurements, Fig. 2 shows lift-off heights for greater dilution levels obtained from temperature measurements in the same flame (described in the next section). Uncertainties in measured lift-off height at higher dilution levels arise from flame asymmetries and are likely responsible for the discrepancies between the two measurement techniques.

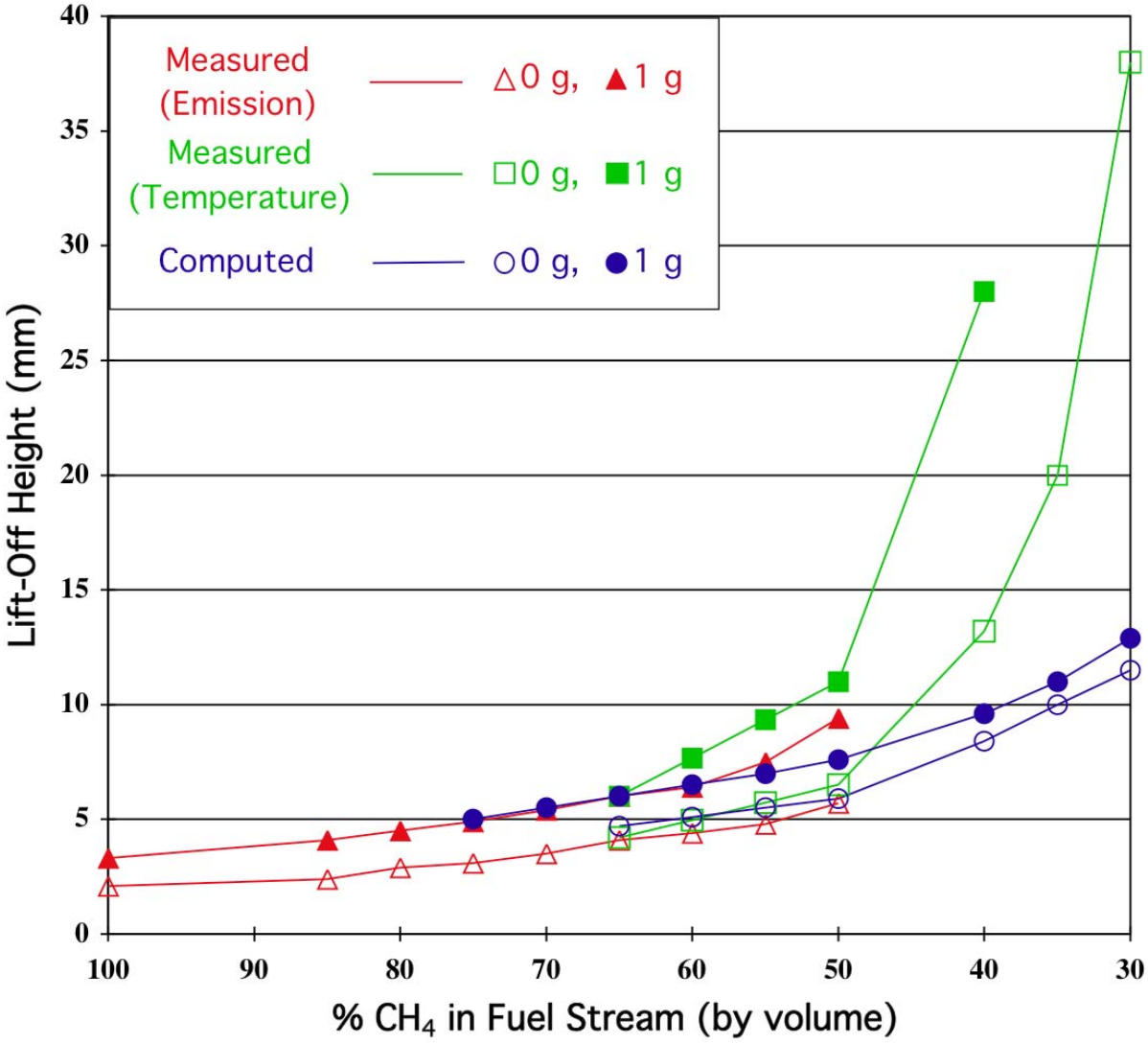

Fig. 2. Measured and computed lift-off as a function of fuel composition.

The predicted lift-off height agrees well with measurement in 1g at the 75/25 and 65/35 fuel mixtures. As the methane level decreases from 65% to 50%, the computed and measured curves begin to separate. When the fuel mixture is diluted below 50% CH_4 in 1 g, the lift-off height becomes increasingly under-predicted, until the code computes a stable flame at fuel mixtures (35% and 30% CH_4) beyond the 1 g experimental blow-off limit (40% CH_4). Further, the difference between computed normal and µg lift-offs does not match the measured curves, which separate increasingly as the fuel mixture is diluted. The measured and computed µg lift-offs show reasonable agreement up to a dilution level of 50% and then depart significantly. The discrepancy between measured and predicted lift-off suggests that there are unresolved kinetic issues, i.e., reaction pathways that may become increasingly important in highly diluted flames that must be studied further in cooler, more dilute methane-air diffusion flames.

1.6 Temperature, Major Species, and Soot Measurements

The chemiluminescence measurements made in our initial µg work characterized flame structure and lift-off over a narrow spatial region. To supplement this information, a series of laser-based measurements was done in four separate measurement campaigns aboard the KC-135. Temperature measurements were performed to allow comparisons between measurement and computation over a larger spatial extent. Likewise, measurements of fuel and oxygen concentrations in the flame-anchoring region provided additional insight into the flow conditions where the discrepancy between measurement and computation was greatest. In addition, two-dimensional laser-induced incandescence (LII) measurements were made to quantify changes in soot concentration and distribution when the influence of gravity is removed. Details of these laser-based measurements along with some of the representative results are given in Appendix A.

1.7 Computations Using Updated Kinetics

The computational models used in our early flame studies included the chemical mechanisms of both GRI-Mech 2.11 and a simple 26-species, C_2 hydrocarbon mechanism developed at Yale. Both mechanisms clearly showed that buoyancy plays a role in both the size and shape of the laminar diffusion flame. The comparisons shown above were done using the 26-species C_2 mechanism, which shows better agreement with measured lift-off than GRI-Mech 2.11 at the 65/35 flow condition. As shown in Fig. 2 above, the agreement in lift-off heights deteriorated rapidly as the dilution level in the flame was increased. Analysis of this disagreement pointed to

a need for improved chemical kinetics. A recent computational effort re-analyzed our standard flames at both normal and zero gravity using a more up-to-date kinetics scheme based on a 66-species C_2H_4 mechanism. The initial results are shown in Fig. 3. Analysis of other dilution levels and the incorporation of our soot model into the calculations are currently underway.

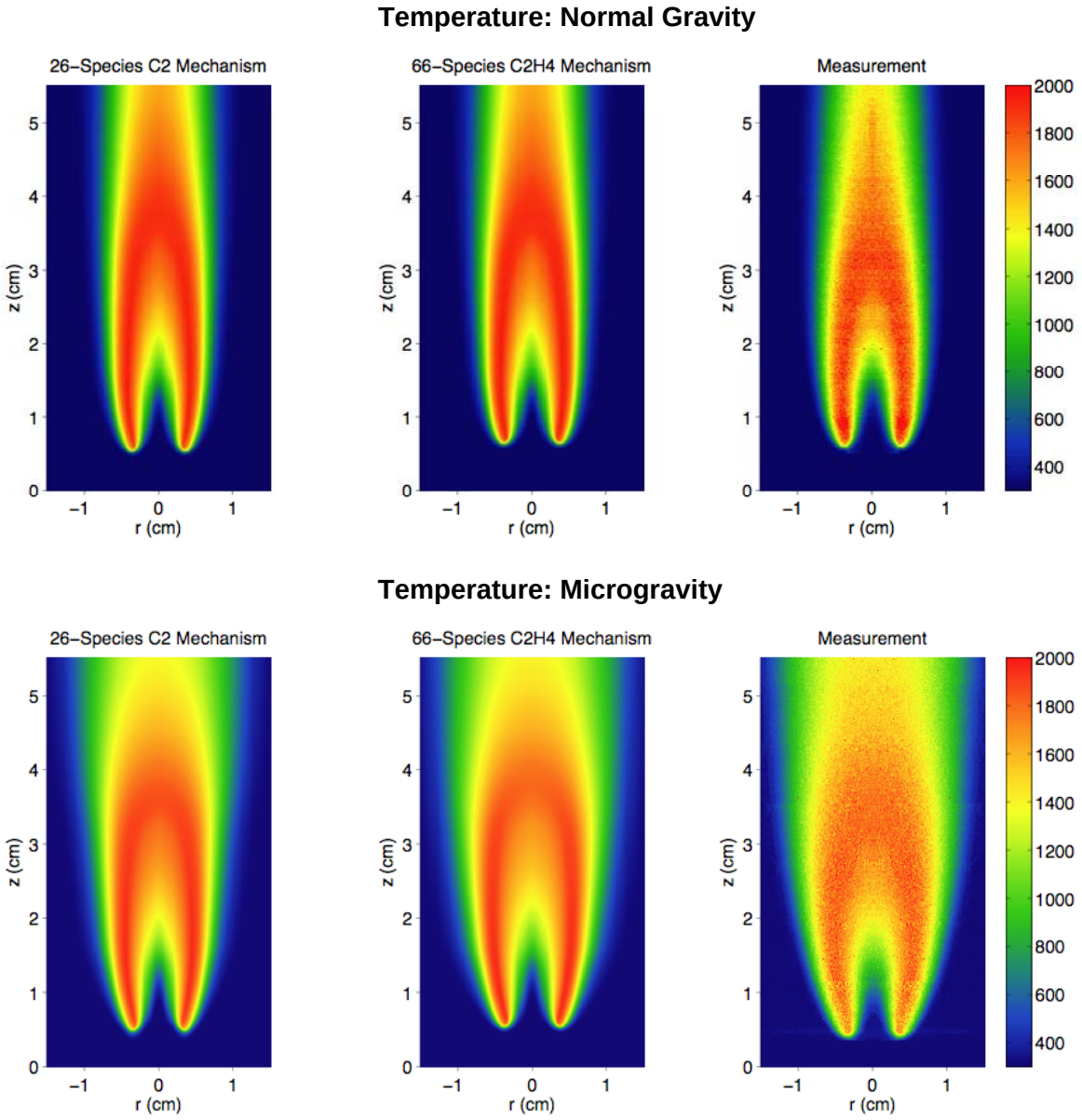

Fig. 3. Calculated and measured temperature profiles. On the left, results of our calculations using a 26-species C_2 mechanism are shown. The middle shows results from a more complete 66-species C_2H_4 mechanism and on the right, temperatures measured using Rayleigh scattering are shown.

2 FLIGHT EXPERIMENT

2.1 Experimental and Computational Project Goals

In our previous NASA-funded research, we have studied computationally and experimentally a series of steady axisymmetric laminar diffusion flames in normal and microgravity environments. Agreement between measured and computed results was good for mildly diluted (and thus nonsooting) flames that we had studied previously in both normal and microgravity. Significant discrepancies became evident, however, when the dilution was increased significantly or when the dilution was decreased and the flame produced soot. The current work will concentrate on flame phenomena at the extremes of the fuel dilution spectrum – namely dilute flames near extinction as well as sooting flames. The project goals of the work will be twofold:

1) Generation and validation of efficient computational techniques, transport and radiation models and modified kinetic mechanisms for hydrocarbon fuels that are able to model effectively diffusion flame structure under a larger parameter range than is currently possible.
2) Development and validation of submodels for soot formation that are capable of predicting both high and low soot loading levels in hydrocarbon flames of various fuels.

To achieve these goals, new data are required that span a larger range of conditions than are currently available. In particular, we plan to obtain data from both methane and ethylene. For each fuel, dilution levels and fuel/coflow velocities will be varied from those causing extinction to those just below the smoke point. The enhanced time and spatial scales in a microgravity environment will allow us to compile a data set that will provide a stringent test for our computational and modeling efforts. As we have shown, microgravity enables the stabilization of flames with increased levels of dilution when compared to normal gravity conditions (Goal 1). The absence of buoyancy also allows the generation of flames that have increased soot residence times compared to ground-based facilities (critical for Goal 2). Thus the ISS should provide an excellent platform from which to understand better the factors that affect diffusion flame lift-off and extinction; it should also provide an excellent test-bed to determine the roles of inception, surface growth and oxidation processes in soot formation models. A recent series of

computations also points to the importance of Soret diffusion in determining the overall distribution of soot in coflow diffusion flames.

Sooting flames are of direct relevance to the study of soot formation/oxidation in turbulent diffusion flames. In particular, turbulent flames are generally nonbuoyant due to their large flow velocities. A microgravity program designed to study soot formation in hydrocarbon flames will increase our understanding of these processes by providing an environment in which we will be able to enhance spatial resolution compared to normal gravity flames and we will be able to adjust the time histories of the soot compared to a normal gravity system, i.e., soot formation and soot oxidation times will be larger for nonbuoyant systems. This will enable detailed complementary studies of benzene production, PAH formation and radical transport to be carried out with the goal of being able to determine the strengths and weaknesses of a variety of soot formation submodels. The soot growth model we will employ couples dynamical equations for particle production to the flow and gaseous species conservation equations. The formulation includes models for the treatment of inception, surface growth, oxidation, and coalescence of soot particulates. Effects of thermal radiation and particle scrubbing of gas phase growth and oxidation species are also included.

2.2 Knowledge Lacking

As outlined in Section 1.5, we have observed that flame lift-off height, overall flame shape, and extinction behavior in coflow diffusion flames have proven to be sensitive tests of the chemical kinetics schemes used to model combustion (see also Fig. 2 above). The availability of microgravity data on these parameters for multiple fuels, and covering conditions that extend to flame extinction will serve as a valuable resource for testing and extending the applicability of chemical kinetics mechanisms. A chemical kinetics scheme that is able to perform well over a larger range of conditions can be expected to do a better job of modeling the full range of behavior encountered in turbulent flames than one that is optimized only for relatively “healthy” flames not close to extinction.

Previous work on soot formation in nonbuoyant environments included both ground-based studies and space based research [25, 28]. That work highlighted the need for longer term, high quality low gravity conditions to characterize accurately the sooting behavior of laminar diffusion flames. The results from those previous studies provide a useful starting point for our own sooting flame investigations. However, the flames in this previous space based work were

anchored on the burner lip, making them much harder to model effectively than the coflow flames to be considered in this study. The completeness of the current soot modeling, the coupling of the soot model to a detailed chemical kinetics mechanism, and the explicit inclusion of radiation effects will make this investigation the most rigorous modeling effort of nonbuoyant soot processes undertaken to date. The proposed microgravity measurements aboard the ISS will provide the experimental data needed to test adequately the fidelity of these current and future soot and radiation models.

2.3 Experimental Objectives

In order to provide the experimental data needed to allow rigorous testing of computational models at the extremes of the fuel dilution spectrum, we have the following objectives:

A) Characterize the behavior of weak coflow diffusion flames of methane and ethylene, as a function of velocity and fuel dilution, through measurement of flame shape, lift-off heights, temperatures and extinction limits.

B) Characterize the sooting tendencies of diffusion flames with long residence times, as a function of velocity and fuel dilution, through measurement of flame shape, gas temperatures in the soot-free portion of the flame, soot luminosity, soot temperatures, and soot volume fractions.

A more complete listing of the specific flame conditions that we will investigate is given in Sections 2.4 and 3.3.

2.4 Summary of Approach

2.4.1 Flame Conditions

We propose to study coflow laminar diffusion flames of methane and ethylene. Fuels will range from pure CH_4 and moderately diluted C_2H_4 (producing sooting, but not smoking flames) to very weak, highly diluted CH_4 and C_2H_4 flames on the verge of extinction. Because of the time required to stabilize these flames and their demonstrated sensitivity to g-jitter, the Combustion Integrated Rack (CIR) aboard the ISS will provide the ideal venue for these experiments.

In an effort to map out the range of flames to be studied at microgravity, we have begun to make measurements of normal gravity flames using a coflow burner that has been designed to be consistent with the bottled gas capabilities of the CIR. Figure 4 shows false-color images of the blue emission from CH_4 flames that cover the range from dilute flames (near extinction) to pure

CH_4 flames, which demonstrate light levels of sooting. Figure 5 shows similar data for C_2H_4 flames, ranging from those the verge of extinction to heavily sooting flames. Both the CH_4 and C_2H_4 flames are studied under a range of dilution levels and flow velocities to produce the desired variation in flame characteristics. It is expected that a number of flow conditions labeled as “unstable at 1g” will be stable under microgravity conditions.

2.4.2 Diagnostic Imaging Techniques

A number of diagnostic imaging techniques will be utilized in the proposed microgravity measurements aboard the ISS. In the following sections, the techniques of color imaging, UV imaging of chemiluminescence, soot pyrometry for temperature and soot volume fraction, thin filament pyrometry for flame temperatures in nonsooting regions of the flame, and laser extinction measurements for soot volume fraction will be discussed.

2.4.2.1 Color Imaging

Color photography from two (and possibly three) different camera systems will be used to monitor the appearance and stability of the flames at the various dilution levels. A color operations (or “ops”) imaging system will provide near real time downlink of the overall flame appearance, while a second (and perhaps third) data color imaging system(s) will provide more quantitative data, though not in real time. The images from the data imaging system can be compared directly with the results of the computations (see Section 2.7 below). Imaging the line-of-sight flame emission from a color digital camera provides information on the flame shape and size, lift-off height, and qualitative distributions of *CH**. We have also recently shown that with proper characterization of the response of the color imaging system, quantitative measurements of gas temperature can be made using thin filament pyrometry, and that measurements of soot temperature and volume fraction are also possible [33].

2.4.2.2 Chemiluminescence

Flame chemiluminescence occurs at 431 nm for *CH** and at 310 nm for *OH**. Both excited species are radicals and are indicative of the flame front [31]. A camera system, capable of detection in the UV, will be used to image emission from *OH** chemiluminescence using an interference filter to isolate the spectral regions of interest. Images of *CH** chemiluminescence are also desired and can be recorded using the data color imaging system being developed for ACME. Because this is a line-of-sight projection technique, data are taken through optics with a low numerical aperture in order to approximate parallel ray collection better. Images are

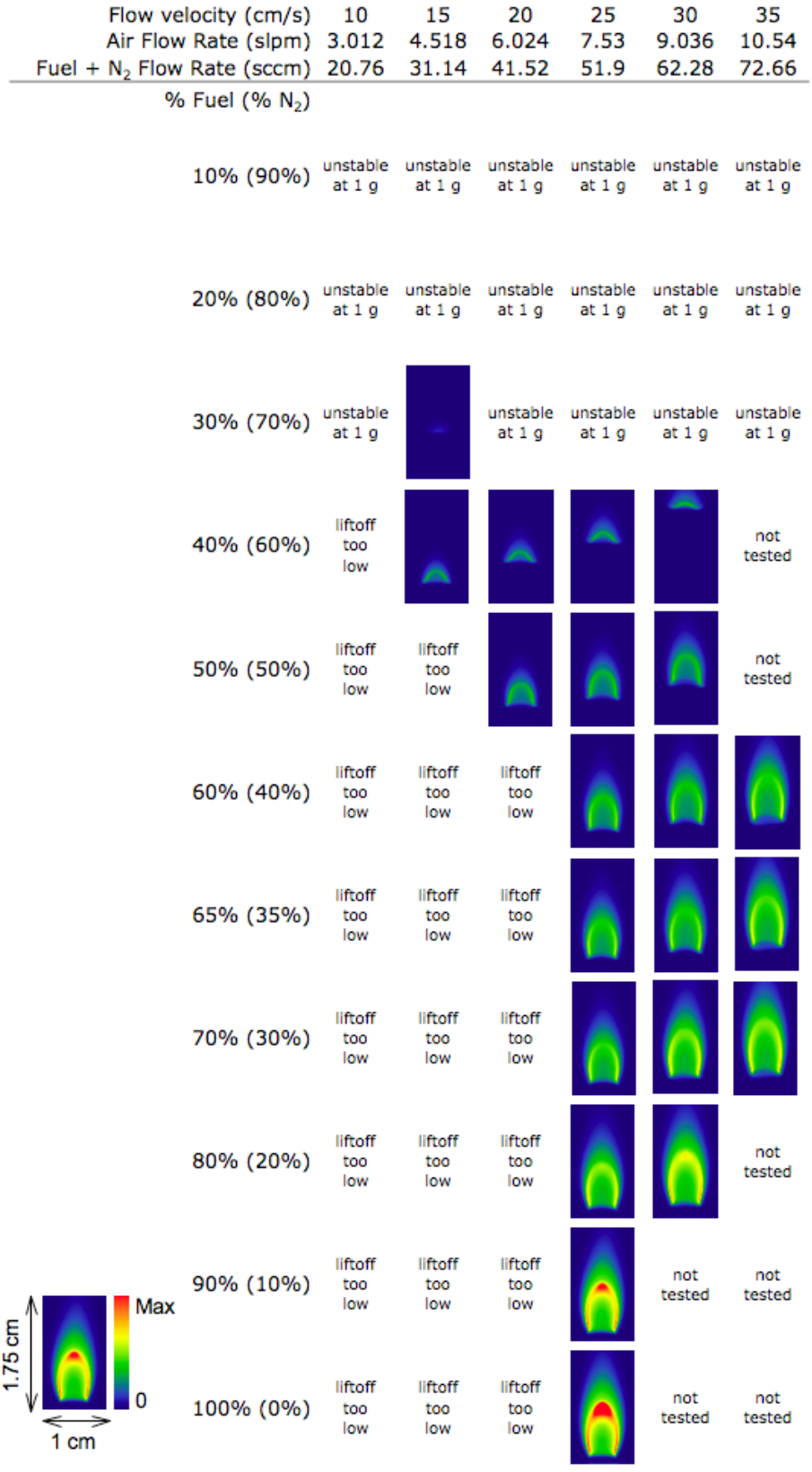

Fig. 4. Flow ranges and some corresponding flame emission images from *CH_4* flames at 1g.

Flow Velocity (cm/s)	**10**	**15**	**20**	**25**	**30**	**31**	**32**	**33**	**34**	**35**
Air Flow Rate (slpm)	3.01	4.52	6.03	7.53	9.04	9.34	9.64	9.94	10.24	10.55
Fuel + N_2 Flow Rate (sccm)	18.85	28.27	37.70	47.12	56.55	58.43	60.32	62.20	64.09	65.97

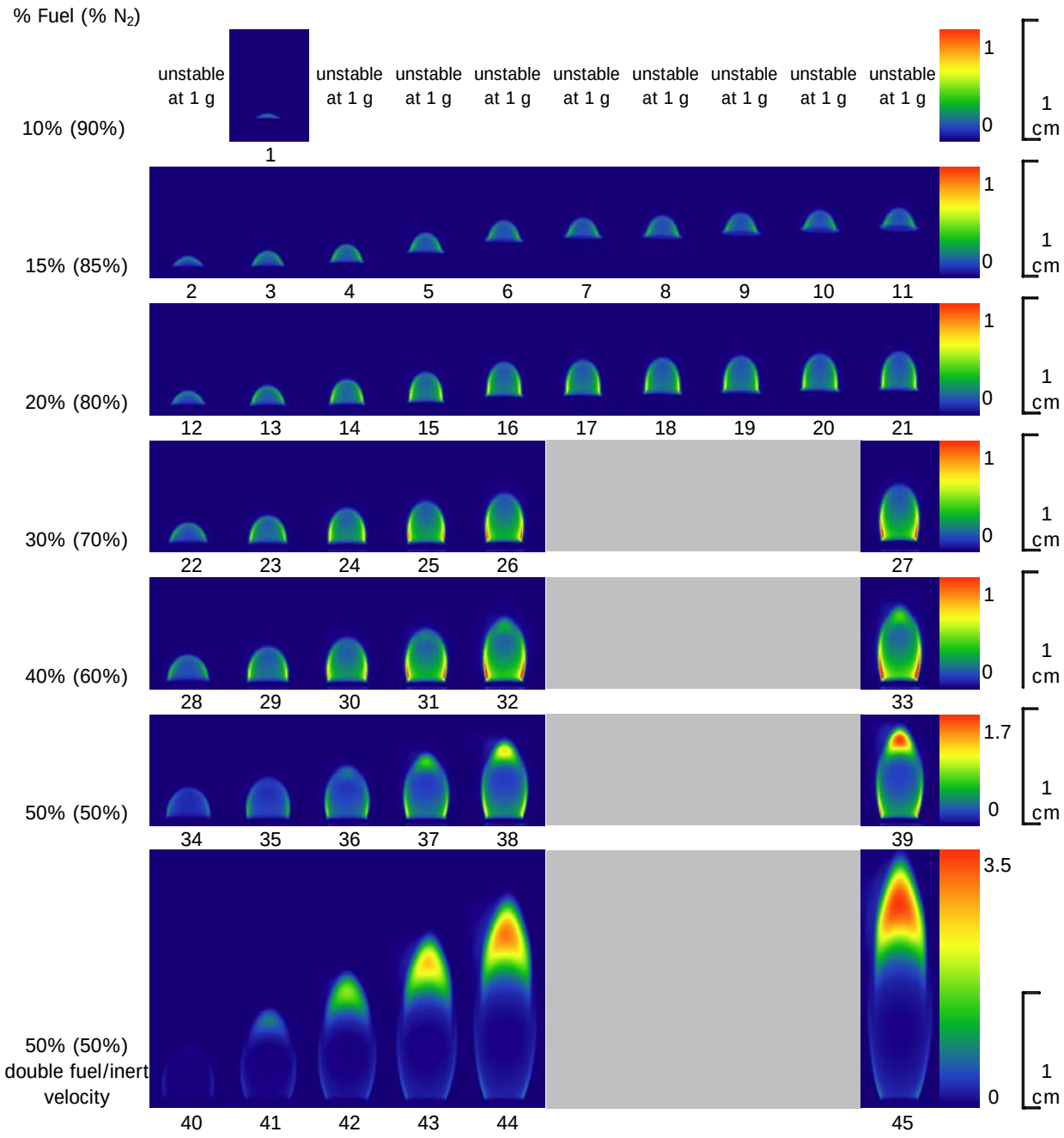

Fig. 5. Flow ranges and some corresponding flame emission images from C_2H_4 flames at normal gravity. In the last row, the fuel/inert velocity are double that of the coflow.

background corrected and tomographically inverted to provide a cross-sectional profile. The *OH** or *CH** images can be used to determine lift-off height and overall flame shape and stability. Our previous work at both normal and μg conditions has shown that *CH** and *OH** are spatially coincident with each other, as well as with the *CH* radical near the base of the flame. Thus we do not anticipate that it will be necessary to monitor both species for all of the flame conditions investigated.

2.4.2.3 Soot Pyrometry

Flame temperatures (in sooting regions of the flames) and soot volume fractions will be determined by imaging the blackbody radiation from the soot. Images of the blackbody radiation can be obtained from either the wide dynamic range CCD detector coupled with a tunable bandpass filter or the data color imaging system. The availability of multiple detection systems to determine temperatures using multi-color optical pyrometry will provide an important check on the accuracy of the measurements. In these experiments, line-of-sight images are acquired at two (or more) wavelengths, a tomographic inversion is applied, and signal ratios between each color image are taken in order to calculate temperatures using the two-color method [34]. The availability of an absolute intensity calibration will further allow the same data to provide a quantitative measurement of the soot volume fraction.

2.4.2.4 Thin Filament Pyrometry

Flame temperatures in nonsooting regions of sooting flames and in dilute flames will be determined using thin filament pyrometry (TFP). In TFP, a silicon carbide (SiC) filament is heated to local temperatures when it is placed at various positions within the flame. The SiC fiber emits blackbody radiation, which is sampled at multiple wavelengths. As with soot pyrometry, the temperature along the fiber is then calculated using two-color pyrometry. Flame temperatures are determined along a radius determined by the fiber, at a single height within the flame. Temperatures can then be determined at multiple heights by using an array of fibers, and/or translating these fibers through the flame. As with the soot pyrometry, either the wide dynamic range CCD/tunable bandpass filter system or the data color imaging system can be used for these measurements.

2.4.2.5 Laser Extinction

The primary determination of soot volume fraction will be obtained using a laser diode illumination package by laser extinction methods. Images will be taken of just the flame to

account for a background correction from flame luminosity, of the laser without the flame, and of the laser passing through the flame. The integrated extinction of the laser beam as it passes through the flame is determined by taking the ratio of the laser image with the flame to the laser image without the flame. This quantity can then be related to the optical thickness of the soot in the flame using the Lambert-Beer law. The soot volume fraction is determined by deconvolution of the line-of-sight signal and using the optical properties of soot for absorption and extinction at the laser wavelength. The radial signal of the optical thickness can then be related to soot temperature [35]. Measurement of the soot volume fraction and soot temperature using the two techniques of pyrometry and extinction will provide a useful consistency check for the soot volume fraction measurements. Once again, we do not anticipate needing to perform both laser extinction and soot pyrometry/volume fraction measurements for all sooting flame conditions.

2.5 Science Data End Products

We will use the experimental techniques summarized in the previous section to investigate a wide range of coflow laminar flame conditions, from very weak flames on the verge of extinction to sooting flames of methane and ethylene. Table 1 summarizes the specific science data end products expected for each of our objectives.

Flame characterization related to Objective A above will concentrate on measurements of nonsooting CH_4 and C_2H_4 flames with dilution selected to range from levels just able to prevent the formation of soot to those high enough to cause extinction. Flame lift-off height and shape will be determined photographically and from measurements of *OH** and/or *CH**. Calibration of the detectors will allow absolute concentrations to be determined, thus providing quantitative comparisons to the computational results. Temperature in these nonsooting flames will be determined from thin filament pyrometry. The wide range of conditions measured experimentally will provide a rich data set for testing the ability of chemical kinetics mechanisms to predict weak flames.

To provide data for the development of soot submodels (Objective B) we will investigate sooting flames of CH_4 and C_2H_4. Once again, a range of dilution levels will be investigated from lightly sooting conditions to those just below the smoke point. Measurements will focus on soot volume fraction (determined by multi-color pyrometry and/or laser extinction) and soot temperature (determined by multi-color pyrometry). Radial temperature profiles at selected nonsooting regions of the flame will be determined using TFP; *OH** and *CH** measurements will

Table 1.

Objective	Science Data End Products
A) Characterize the behavior of weak coflow diffusion flames of CH_4 and C_2H_4, as a function of velocity and fuel dilution.	A1: Color images of nonsooting flames with varying dilution levels and lift-off heights for both fuels. A2: 2D images of *OH** (and *CH**, desired) concentration for selected flow conditions for both fuels. A3: Peak concentration of *OH** (and *CH**, desired) as a function of fuel dilution for flames at various flow velocities for both fuels. A4: Lift-off height as a function of fuel dilution for flames at various flow velocities for both fuels. A5: Flame length and width as a function of fuel dilution at various flow velocities for both fuels. A6: Dilution level at extinction as a function of velocity for both fuels. A7: Radial temperature profiles for selected flow conditions for both fuels. A8: Peak temperature as a function of fuel dilution for varying flow velocities for both fuels.
B) Characterize the sooting tendencies of CH_4 and C_2H_4 diffusion flames with long residence times, as a function of velocity and fuel dilution.	B1: Color images of sooting flames with varying dilution levels for both fuels. B2: 2D images of *OH** (and *CH**, desired) concentration for selected flow conditions for both fuels. B3: Peak concentration of *OH** (and *CH**, desired) as a function of fuel dilution for flames at various flow velocities for both fuels. B4: Lift-off height as a function of fuel dilution for flames at various flow velocities for both fuels. B5: Flame length and width as a function of fuel dilution at various flow velocities for both fuels. B6: Dilution level for first appearance of soot as a function of velocity for both fuels. B7: Dilution level at smoke point (if any) as a function of velocity for both fuels. B8: Radial temperature profiles for selected flow conditions for both fuels. B9: 2D images of soot temperature for selected flow conditions for both fuels. B10: Peak soot temperature as a function of fuel dilution for varying flow velocities for both fuels. B11: 2D images of soot volume fraction for selected flow conditions for both fuels. B12: Peak soot volume fraction as a function of fuel dilution for varying flow velocities for both fuels.

be made at the base of the flames. Each measured quantity will be compared with computational predictions. Because of the longer time scales in soot-producing regions (compared to those at normal gravity), the data are expected to be a stringent test of the soot model. Discrepancies between measurements and computations over this range of conditions are expected to suggest refinements to the soot model that will improve our ability to predict soot in momentum-dominated nonpremixed combustion systems.

2.6 Justification for Extended-Duration Microgravity

The ability to predict the coupled effects of complex transport phenomena with detailed chemical kinetics in diffusion flames is central to nearly all aspects of combustion research: in the modeling of turbulent reacting flows, in understanding the processes by which soot formation and radiative transfer take place, and in the prediction of pollutant formation. In addition, an understanding of those factors that affect flame extinction is critical in the suppression of fires, in improving engine efficiency, and in reducing emissions. While normal gravity combustion studies can provide important information on combustion processes, the effects of gravitational forces can often complicate the interpretation of both computational and experimental results. For example, most practical combustors are turbulent, and consequently momentum-dominated, while most laboratory-scale research burners have significant buoyancy contributions. Therefore, studies of microgravity flames are of direct relevance to research in turbulent combustion since buoyancy effects are eliminated. In addition to being inherently simpler, nonbuoyant flames have the advantage that hot gases are not accelerated by gravitational forces, which results in longer residence times and larger length scales. These longer residence times have been shown to result in higher soot loading in microgravity flames compared to their normal gravity counterparts. The larger spatial scales allow improved experimental resolution, which in turn gives a clearer, more spatially distinct view of the progress from soot inception and growth to eventual burnout. Thus, microgravity data on sooting flames will provide a wide range of well-resolved conditions that will be critical for the development of submodels for soot formation that are capable of predicting both high and low soot loading levels.

As we have seen from our previous microgravity work (see Fig. 2), very weak flames can be stabilized in a microgravity that extinguish under normal gravity conditions. These flames are free of buoyant coupling of the flowfield or buoyancy-induced asymmetries, which can

complicate comparisons between models and experiments under normal gravity conditions. For these flames, small changes in the chemical kinetics were seen to have a significant effect on the agreement between measured and computed flame structure and lift-off height. Once again, the microgravity environment allows us to investigate a wider range of flow and dilution conditions than would be accessible in a normal gravity environment; these data will be invaluable for our overall goal of developing improved kinetic mechanisms applicable to a wide range of combustion conditions.

Section 1 discusses our previous experimental work in microgravity, which was carried out aboard the KC-135. The KC-135 was chosen over other ground-based microgravity facilities (such as a drop towers) due to the relatively long periods of microgravity available, which allowed adequate time for flame stabilization and integration of weak signals necessary for good signal/noise. However, the work also showed that both very dilute flames near extinction and sooty flames are sensitive to the g-jitter aboard the KC-135.

Highly dilute fuel mixtures, which can only be stabilized under microgravity conditions, cannot be lit until microgravity conditions are reached. After ignition is established, the ignition source must be removed, and the flame allowed to stabilize. Further, data acquisition of flame chemiluminescence requires total integration times of ~10 seconds to obtain sufficient signal/noise for good results when a tomographic inversion is used to reconstruct a two-dimensional cross section. Because flame luminosity is integrated along a line-of-sight, a low numerical aperture must be used, which results in a small optical throughput. The combination of the time requirements for flame ignition, stabilization, and signal integration makes this experiment a poor candidate for drop tower facilities. The most dilute of these mixtures previously studied exhibited unstable behavior aboard the KC-135 similar to that observed for sooting flames, with the lift-off height changing by several mm over the course of a parabola. The longer periods of comparatively jitter-free μg available on the ISS will be critical for quantitative characterization of these weak flames. A better understanding of the limits of extinction in these relatively cool flames will be important for improving kinetics mechanisms and understanding pathways to extinction. Additionally, longer uninterrupted periods of microgravity will provide the opportunity to study a wider range of flow conditions without having to reset the experimental apparatus.

For sooting flames, a number of experiments have shown that the overall flame structure is markedly different in space than in the shorter-duration periods of microgravity available in ground-based facilities [9]. Candle flames that were sooty in normal gravity, during aircraft testing, and in the high-quality microgravity of drop facilities, were observed to be blue in testing on orbit in the Space Shuttle and Mir space station [36, 37]. If the experimental results obtained are to be used to validate the soot models, the long-term, low-jitter environment of space will be required.

2.7 Computational Research Plan

We will carry out a closely coupled experimental and computational research program. Our previous experience has shown that it is critical to ensure that the boundary conditions for the burner are well known to allow meaningful comparisons with the computational models. Indeed, a major advantage of the coflow flame configuration is that the flame can be lifted off of the burner face, thus eliminating the need to model the degree of heat loss to the burner.

We have begun a detailed set of measurements in normal gravity conditions to characterize a coflow burner with the same properties as the one that will be used in the CIR. Once the boundary conditions are fully characterized, computations will begin on this new series of flames. An advantage of the coupling of a detailed computational model with experimental measurements is the ability of the computations to make meaningful comparisons to even relatively simple diagnostics measurements (such as will be available on the ISS). As an example of this, Fig. 6 shows simulated flame images from 40% C_2H_4 / 60% N_2 and 80% C_2H_4 / 20% N_2 flames. The computations used an axisymmetric computational model that employed the gas-phase diffusion flame equations in the velocity-vorticity formulation with buoyancy and the particle sectional approach presented in Ref. [38]. The gas and soot equations are additionally coupled through nonadiabatic radiative loss. Radial and axial velocities, the vorticity, the temperature, the gas-phase species and the particle sectional mass fractions are computed. The chemical mechanism was derived from one of the more comprehensive and well-validated sets available for ethylene [39]. The resultant mechanism contained 476 reactions and 66 chemical species. Twenty soot sections are included in the formulation. The result is a model that requires a total of 90 dependent variables to be solved at each grid point. The system is closed with the ideal gas law and appropriate boundary conditions are applied on each side of the computational domain. Local properties are evaluated via transport and chemistry libraries. The sectional

thermophoretic velocities in the free molecule regime are given in Ref. [38] as are the sectional diffusion velocities written with a mass-weighted mean diffusion coefficient for each size class. The governing conservation equations are solved on a two-dimensional mesh by combining a Newton-based steady-state and a time-dependent solution method [40]. A time-dependent solution is first obtained on a coarse grid and then grid points are inserted adaptively to increase the resolution in regions of high spatial activity. Computations were performed on an AMD Dual Opteron 240 system running at 1.4 GHz.

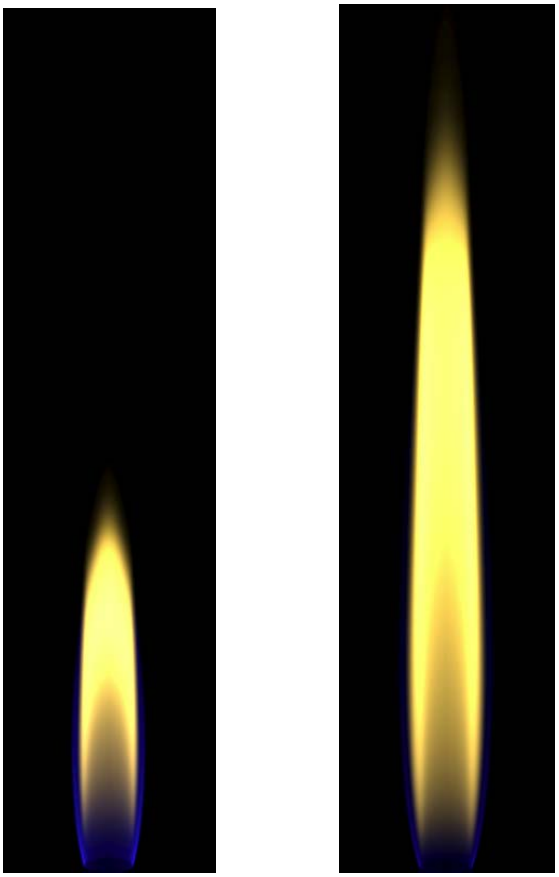

40% C_2H_4 **80% C_2H_4**

Fig. 6. Simulated flame images based on the calculated soot volume fraction, temperature, and *CH* number density. The two-dimensional profiles were rotated about the symmetry axis to get a three-dimensional intensity distribution and realistic camera parameters were used to calculate the image.

The detailed soot model allowed determination of the overall soot volume fraction as well as the temperature. The two-dimensional profiles were rotated about the symmetry axis and combined with Planck's law to get a three-dimensional intensity distribution as a function of wavelength. By convolving this intensity distribution with measured filter profiles for the red,

green, and blue filters used in a digital camera, it was possible to simulate the flame image from the soot. The spatial distribution of *CH* was used to simulate the chemiluminescence from *CH** at the base of the flame, since the mechanism used here did not include *CH** chemistry. However, our previous work has shown that the two distinct species are spatially coincident in the flame [30]. Future computations can be easily modified to include the kinetics for chemiluminescent species, which have been improved significantly in recent years [31].

Beyond the acquisition of data from a wide range of dilution levels for both methane and ethylene, a valuable end product of the research will be the results of the computations, with their detailed chemical mechanisms, soot modeling, and complex transport. Based on observations, modifications can be made to the kinetics and soot model to match better the experimental results. If the overall agreement of the measurements and computations is good, the results of the computations can be "mined" to provide insight on species (and hence chemical processes) that cannot be measured directly using the diagnostics available for the proposed experiment.

3 EXPERIMENT REQUIREMENTS

3.1 Requirements Discussion

This section does not include any requirements, but instead describes their importance in achieving the experiment objectives. The requirements have been incorporated into the merged ACME Science Requirements.

3.1.1 Coflow Burner Configuration

There are a number of factors that must be considered when planning an experiment to be run on the ISS. The burner configuration and experimental plan must be compatible with the CIR. The burner used in previous studies required flow rates as high as 43 liters/min for the coflow, and 0.3 liters/min for the fuel flow. Due to the limited amount of gases available on the ISS, it is desirable that the experiment involve as low flow rates as possible. However, simply decreasing flow rates while using the same burner as in our previous experiments would result in smaller lift-off heights, increasing heat transfer from the flame to the burner (which is difficult to quantify and model). Instead, we have proposed reducing the diameter of our normal burner by a factor of two, making it possible to reduce flow rates significantly while maintaining a flame that is similar in composition to the flames imaged in earlier studies. In its proposed configuration,

the burner will have a coflow with an outer diameter of 25 mm and a circular central tube of 2.1 mm inside diameter with a wall thickness of 0.13 mm.

To conserve gas supplies, it is also important that the changeover time between different flow conditions be minimized. The volume of the central fuel tube inlet plenum must therefore be minimized. The volume of the fuel/inert mixture between the mass flow controllers and burner outlet must be completely flushed when switching between flow conditions that use different ratios of fuel to inert.

3.1.2 Gases Required

Four source gas compositions are required in order to investigate the flames outlined in Section 3.3: CH_4 (fuel), C_2H_4 (fuel), 21% O_2 / 79% N_2 (air), and N_2 (inert). Investigating both CH_4 and C_2H_4 flames with various levels of N_2 dilution will allow us to test different hydrocarbon fuels, while still utilizing reasonably well established and computationally tractable chemical kinetics mechanisms. The average velocity of the fuel and coflow streams will be matched for most of our test cases. A range of velocities will be measured in order to investigate different flow/chemistry regimes. The use of a mixture of 21% O_2 / 79% N_2 for the coflow will make the results relevant to standard fuel/air combustion systems, and will ensure an accurate knowledge of the O_2/N_2 ratio that would not be available if the constituent coflow gases were mixed using the CIR flow controllers. This accuracy will be important for comparisons with the computational results.

3.1.3 Ambient Environment

Because the combustion vessel in the CIR will be sealed during the experiment, an increase in pressure in the vessel is expected, primarily due to the coflow. Even with the reduced flow rates achieved with the current burner specification, total flow rates as high as 11 liters/min must still be used. Appendix B details the expected pressure rise in a sealed chamber for a variety of flow conditions. Briefly, the gas in an 80 liter chamber is modeled as an ideal gas; increases to the chamber pressure are calculated by including the increase in mass in the chamber due to gas flow from the burner and increase in chamber temperature due to flame heating.

For an initial flow velocity of 35 cm/s, the pressure is found to increase at a rate of 0.137 bar/min (Figs. B1 and B2), while the temperature is found to increase at a negligible rate of 0.2 K/min (Fig. B3). A typical run time of ~4-5 min. (see Section 3.2) at the maximum coflow velocity would result in an overall pressure increase of 0.55-0.69 bar and a temperature

increase of 0.8 K. Additionally, the soot levels in the flames have been found to increase by as much as a factor of 2 with an increase in pressure of approximately 0.3 bar. A more detailed discussion on how this increase in pressure increases soot production is included in Appendix C. The measured pressure will be monitored and the computations will be modified to take the increasing pressure into account.

3.1.4 Science Diagnostics Requirements

In order to characterize properly the coflow flames under investigation, a number of imaging systems will be used. An imaging system capable of measurements into the UV will allow measurement of *OH** distributions as well as overall flame structure, lift-off height, and extinction limits. *OH** distributions can be measured through an interference filter at 310 nm and *CH** distributions can be measured using the data color imaging system. Blackbody calibration of the new detectors is to be carried before the experiment is placed on the ISS. If the calibration is available, a spectral overlap correction will be performed to obtain quantitative number densities of *CH** and *OH**.

As described in Sect. 2.4.2.1, color photography will be used to monitor the appearance and stability of the flames at the various dilution levels. The detector on a digital camera combines the usual intensity detector of a scientific CCD or CMOS chip with a patterned color filter array (CFA) arranged over the chip's pixels. The CFA allows for spectral flame emission sampling at the red, green, and blue filters of the CFA. *CH** emission is sampled by the blue channels, while the blackbody emission from the soot is sampled by all three-color channels. The combined signals from all three channels provide a color image and, as demonstrated in Section 2.7 above, can be compared with the results of the computations. Calibration of the camera has been demonstrated to allow quantitative measurements [33].

A third imaging system will consist of a high dynamic range detector coupled with a tunable filter. This system will be used for several different measurements. Sampling soot luminosity at different wavelengths using the tunable filter will provide the information necessary to determine soot temperatures and soot volume fractions using multi-color pyrometry [34]. As with the chemiluminescence measurements, data are taken with low numerical aperture optics for a better approximation to the assumption of parallel ray collection. A blackbody calibration of the camera will allow calculation of the soot volume fraction from the derived soot temperature distribution and the measured intensity distribution of soot luminosity [35, 41]. Temperatures in

the soot free regions of the flame can be determined using two-color thin filament pyrometry (TFP). Measurements at different downstream regions in the flames will be obtained by translating a single SiC filament (or an array fibers) through the flame. The soot volume fraction can also be measured using the high dynamic range camera in conjunction with a laser diode illumination package. Temperatures in the range of 1200-2100 K (±50 K), and soot volume fractions within 0.1-20 ppm (±0.05 ppm) should be within the measurement capabilities of the apparatus. The uncertainty listed for the soot volume fractions does not take into account variations in the soot absorption function or the extinction coefficient, which are known to vary by as much as 20%.

Due to the small size of our coflow flames (2 mm fuel jet diameter) and the narrow profiles of some of the features that we wish to measure (e.g., *CH** and *OH** layers are typically ~0.1 mm thick), a relatively high spatial resolution is required. Flames generated with the coflow burner are expected to have a luminous region no larger than 1.5 cm tall by 0.6 cm wide, and will often be smaller near the extinction limits (see Figs. 4 and 5 for illustration). The highest spatial resolution can be achieved by filling the imaging detector as much as possible with the flame region. Therefore, we require that the optics with the smallest available field of view be used for our experiments. Ideally, each camera would view the area within 10 mm of the burner axis (i.e., 20 mm diameter), centered on the burner axis, extending from the burner outlet to 25 mm downstream of (i.e., above) the central fuel tube. This measurement region, imaged on a 1024x1024 CCD detector (consistent with the detectors available), corresponds to a spatial resolution of 0.05 mm, using Nyquist sampling criteria.

3.2 Operational Sequence

The main goal of this experiment is to evaluate flame characteristics at the extremes of fuel dilution: both weak, highly-dilute flames, and sooting flames up to pure-fuel conditions. While such parameters as the extinction limits and potential smoke points within these flames can easily be determined in normal gravity, we will not know the exact microgravity limits until the experiment is run on the ISS. We therefore plan to execute an initial run for each fuel where we vary the flow velocities and dilution levels in order to determine the extinction limits and degree of soot production in microgravity. For extinction limits, the flow velocity will be slowly ramped until extinction is observed for a given dilution level. The dilution level will then be increased in

5% increments and the procedure repeated. Extinction can be detected quickly with a PMT, but the color imaging system, HiBMs camera, and ops imaging system will all be run during these scans to maximize the data collected. For sooting determination, the dilution level will be decreased in 5% increments and/or the flow velocity will be increased in 5 cm/s increments until soot is observed, and then continued until either a smoke point is reached or a predetermined upper limit is reached. These observations can be made using the ops and color imaging systems. Table 2 outlines the procedure to determine the extinction limits of the flames as well as identify any smoke points for the C_2H_4 flames. Based on the results of these scans, the exact test matrix can be modified as necessary for further runs.

Due to the large number of conditions to be tested and the limited amount of gases available (as many as 50+ conditions for each fuel), it is necessary to minimize the test time, while exploring as many conditions as possible. One experimental concern involves the stabilization time necessary to change between different flow conditions, specifically when changing the ratio of fuel to inert. To minimize this time, the mixture ratio will be held fixed and the exit velocity will be varied. Varying the exit velocity has been observed to produce a steady flame within seconds. This improvement allows for data acquisition on the next test condition to begin without having to wait, minimizing the time necessary to navigate the range of flow conditions under investigation (see Section 3.3 for a detailed list of flow conditions under investigation).

Experiments in the coflow flame will be carried out in the order laid out in Table 3. They will follow one of two sequences: (a) varying flow conditions towards extinction, or (b) varying flow conditions to a sooting condition. First the chamber will be filled to a pressure of one atmosphere. Normal gravity tests of our 25 mm diameter coflow flames in an enclosed 43-liter chamber filled with argon indicate that the fill gas is not critical, since the coflow provides the local environment for the flame. However, under microgravity conditions, the flames could exhibit greater sensitivity to the fill gas. To investigate this, our first exploratory test for methane extinction will be carried out twice – once with air, and a second time with ambient nitrogen. Once the ambient environment is set, the igniter will be inserted and the coflow and fuel/inert flow will begin at predetermined ignition conditions. Once ignition is detected the igniter will be removed and the flow conditions set to the starting point of a particular experimental run. Ideally, the fuel dilution level used for a single run would also be used for ignition; however, in the more dilute cases removal of the igniter from the flame is anticipated to extinguish the flame.

Therefore, those runs will begin in the moderately-dilute (or healthy) flame range for ignition purposes. The fuel dilution will be adjusted to the initial test case (if necessary) and then data acquisition will be carried out at the different fluid velocities until extinction is detected. The chamber will be vented to 1 bar after each data acquisition. Once the extinction limit is reached for a particular dilution level, the flow conditions will be reset to a healthy ignition setting and reignited.

Table 2.

Exploratory test procedures to determine final test limits.	
Extinction Limit Test	**Approx. Start Time**
1. Prepare chamber atmosphere	
2. Start coflow and fuel/inert flow at TBD ignition condition (e.g., a 40% CH_4 flame or a 20% C_2H_4 flame)	0 sec.
3. Ignite flame and retract igniter	10 sec.
4. Slowly ramp flow (0.5 cm/s^2) to starting velocity, if needed	20 sec.
5. Begin scan for a specific dilution: Increase velocity at a rate of 0.5 cm/s^2	30 sec.
6. Stop test when extinction is detected by PMT or 50 cm/s is reached	110 sec.
7. Extinguish flame and vent the chamber to 1 bar	
8. Reduce fuel concentration by 5% and repeat steps 2-7 for the next dilution	
9. Keep reducing fuel concentration by 5% and repeating steps 2-7 until minimum fuel concentration (see test matrix in Tables 4 and 5) is reached	
10. Reset apparatus	
Sooting Limit Test (for smoke point of ethylene flames)	
1. Prepare chamber atmosphere	
2. Start coflow and fuel/inert flow at TBD ignition condition (e.g., a 40% C_2H_4 flame)	0 sec.
3. Ignite flame and retract igniter	10 sec.
4. Ramp flow velocity (TBD) to 40% C_2H_4, 10 cm/s	20 sec.
5. Begin scan of 40% C_2H_4: Increase velocity at a rate of 0.5 cm/s^2	30 sec.
6. Stop test when 35 cm/s is reached	80 sec.
7. Extinguish the flame and vent chamber to 1 bar	
8. Ignite flame, retract igniter, and ramp flow velocity (TBD) to 45% C_2H_4, 10 cm/s	
9. Begin scan of 45% C_2H_4: Increase velocity at a rate of 0.5 cm/s^2	
10. Stop test when the velocity reaches the smoke point determined in the previous run, or 35 cm/s	
11. Extinguish the flame and vent chamber to 1 bar	
12. Repeat steps 8-11for 50% C_2H_4	
13. Repeat steps 8-11 for 50% C_2H_4, double fuel velocity	
14. Reset apparatus	

Table 3.

Coflow Laminar Diffusion Flame Overall Operational Sequence.	
Action	**Approx. Start Time**
1. Take reference images	-5 min.
2. Fill/scrub/vent chamber to 1 bar	
3. Start coflow and fuel/inert flow at ignition condition	0 sec.
4. Ignite flame and retract igniter	
5. Ramp flow velocity (TBD) to initial test condition, if needed	10 sec.
6. Wait for flame to stabilize	20 sec.
7. Run data acquisition	
8. Extinguish flame	30 sec.
9. Repeat 2 to 8 until (10 cases each run):	
a) the extinction limit	
b) the sooting extreme	
Limits determined from exploratory tests.	
Continue at next dilution for test duration	
10. Take reference images, if applicable	
11. Downlink data	
12. Reset apparatus	

The (a) and (b) sequences may require somewhat different exposure times, as chemiluminescence images (a) require up to 10 second exposure lengths, and soot luminosity images (b) will saturate in less than one second for highly sooting flames. During the sooting experiments, chemiluminescence images will still be acquired and will be the determining factor for the total amount of time necessary for data acquisition at each test condition. Since the exposures used for the soot luminosity images are so much shorter than the chemiluminescence images, it will be possible to take exposures at several settings of the tunable color filter (for multi-colored pyrometry) in the same span of time. Similarly, it will be possible to take data with both the laser on and laser off at each flame condition for laser extinction and to translate the TFP array through the flame. The general assumptions made in calculating the times required for recording a single flame condition are that it will take 15 seconds for a single data acquisition cycle and 10 seconds to change flow conditions and allow the flame to stabilize. Since both our normal gravity and microgravity experiments on the KC-135 indicate that these flames will be stable, we anticipate reducing the framing rate of the imaging systems to optimize signal/noise and limit the amount of data that must be downloaded. We anticipate that framing rates of 7.5 – 10 frames per second will be sufficient for all of our flames.

3.3 Test Matrix

Once the full range of flow conditions to investigate has been determined using the initial exploratory procedure to establish extinction and sooting smoke-point limits, the plan for additional test cases will be finalized. Test matrices detailing the range of flames to be tested in the exploratory tests (using the procedure laid out in Table 2) are provided in Tables 4-6. Exploratory tests to determine the extinction limits of CH_4 and C_2H_4 are provided in Tables 4 and 5, respectively. Table 6 presents the tests to determine the smoke points (if any) of the C_2H_4 flames. Table 7 outlines a detailed preliminary test matrix for the CH_4 flames, and Table 8 outlines a detailed preliminary test matrix for the C_2H_4 flames. These test matrices have been laid out using observations of these flames at normal gravity coupled with the expectation that there will be a wider range of flames that can be stabilized under microgravity conditions. Experimental runs have been split up into groups of ~10 tests so that a run will last ~4-5 min. Dilution levels with fewer test cases have been grouped together in an effort to minimize the number of times the experimental apparatus will have to be reset.

The test matrices were created with two goals in mind: to investigate weak, dilute flames as they approach extinction, and to investigate the sooting tendencies of richer flames. In all cases, flames are lifted off the burner surface so that heat transfer to the burner can be neglected in the computations. This approach has been observed to work well for all cases of the methane flames, whereas moderate heating of the burner surface has been observed for some cases of the ethylene flames. The laminar flame speed of ethylene is higher than that of methane, causing lift-off heights to decrease by approximately a factor of two. For nonsooting flames, this decrease in lift-off height does not create any burner heating. However, the more heavily sooting cases have been observed to cause moderate heat transfer to the burner, which becomes a problem in the ethylene flames since they have a higher propensity to soot, particularly at microgravity. The 50% C_2H_4 / 50% N_2 flame has been observed to be the lowest level of dilution that ensures the room temperature boundary condition at the burner surface to be a good assumption for the computations. By increasing the fuel flow rate by a factor of 2 (as shown in Test #'s 106-111 in Table 6), the overall amount of soot and the size of the sooting region are increased (at 1 g), with the sooting region substantially higher off the burner surface to prevent burner heating. Raising the sooting region further off the burner surface becomes more important under microgravity conditions as the lift-off height decreases relative to 1 g conditions due to the increased importance of axial diffusion.

Table 4. Test matrix for exploratory tests of the extinction limits of methane. To verify the insensitivity of the flames to the ambient environment, this will be carried out twice – once with air, and a second time with ambient nitrogen.

Run	Test #	% CH_4 (% N_2)	Flow Velocity	Test type	Comments
A	1	40% (60%)	15 cm/s - 50 cm/s	extinction detection	Initial run; ambient will be air. Chemiluminescence will be monitored using a PMT to determine the velocity that causes extinction at this dilution level. The flow velocity will begin at 15 cm/s and will be ramped slowly at 0.5 cm/s^2 until extinction is detected, or 50 cm/s is reached.
	2	35% (65%)	15 cm/s - 50 cm/s	extinction detection	Same as above.
	3	30% (70%)	15 cm/s - 50 cm/s	extinction detection	Same as above.
	4	25% (75%)	15 cm/s - 50 cm/s	extinction detection	Same as above.
	5	20% (80%)	15 cm/s - 50 cm/s	extinction detection	Same as above.
	6	15% (85%)	15 cm/s - 50 cm/s	extinction detection	Same as above. *There may not be a stable flame at this dilution level.*
B	1	40% (60%)	15 cm/s - 50 cm/s	extinction detection	Duplicate run; ambient will be nitrogen. Chemiluminescence will be monitored using a PMT to determine the velocity that causes extinction at this dilution level. The flow velocity will begin at 15 cm/s and will be ramped slowly at 0.5 cm/s^2 until extinction is detected, or 50 cm/s is reached.
	2	35% (65%)	15 cm/s - 50 cm/s	extinction detection	Same as above.
	3	30% (70%)	15 cm/s - 50 cm/s	extinction detection	Same as above.
	4	25% (75%)	15 cm/s - 50 cm/s	extinction detection	Same as above.
	5	20% (80%)	15 cm/s - 50 cm/s	extinction detection	Same as above.
	6	15% (85%)	15 cm/s - 50 cm/s	extinction detection	Same as above. *There may not be a stable flame at this dilution level.*

Table 5. Test matrix for exploratory tests of the extinction limits of ethylene.

Run	Test #	% C_2H_4 (% N_2)	Flow Velocity	Test type	Comments
C	1	20% (80%)	10 cm/s - 50 cm/s	extinction detection	Chemiluminescence will be monitored using a PMT to determine the velocity that causes extinction at this dilution level. The flow velocity will begin at 10 cm/s and will be ramped slowly at 0.5 cm/s^2 until extinction is detected, or 50 cm/s is reached.
	2	15% (85%)	10 cm/s - 50 cm/s	extinction detection	Same as above.
	3	10% (90%)	10 cm/s - 50 cm/s	extinction detection	Same as above. *There may not be a stable flame at this dilution level.*

Table 6. Test matrix for exploratory tests of the smoke points of ethylene.

Run	Test #	% C_2H_4 (% N_2)	Flow Velocity	Test type	Comments
D	1	40% (60%)	10 cm/s - 35 cm/s	smoke point detection	The sooting tendency of the flames will be monitored with color photography. The flow velocity will begin at 10 cm/s and will be ramped slowly at 0.5 cm/s^2 until 35 cm/s is reached.
	2	45% (55%)	10 cm/s - 35 cm/s	smoke point detection	The sooting tendency of the flames will be monitored with color photography. The flow velocity will begin at 10 cm/s and will be ramped slowly at 0.5 cm/s^2 until 35 cm/s is reached, or to the the smoke point observed in the previous run.
	3	50% (50%)	10 cm/s - 35 cm/s	smoke point detection	Same as above.
	4	50% (50%) (double-velocity fuel flow)*	10 cm/s - 35 cm/s	smoke point detection	Same as above.

* In Test # D4 above, the flow velocity of the fuel and inert are doubled to twice the value listed in the “Flow Velocity” column. The coflow is still run at the velocity listed.

Table 7. Test matrix for methane.
Note: v(bo) is the velocity at blow off determined from exploratory tests

Run	Test #	% CH_4 (% N_2)	Flow Velocity	Test type	Comments
1	1	15% (85%)	10 cm/s	a) extinction/	Chemiluminescence will be monitored
	2		15 cm/s	lifted	to determine the lift-off height and
	3		20 cm/s		extinction limit.
	4		25 cm/s		Tests may be removed from (or added
	5		30 cm/s		to) this run based on the initial
	6		v(bo)-4 cm/s		exploratory test.
	7		v(bo)-3 cm/s		*There may not be a stable flame at*
	8		v(bo)-2 cm/s		*this dilution level.*
	9		v(bo)-1 cm/s		REQUIRED
	10		v(bo)-0.5 cm/s		
2	11	20% (80%)	10 cm/s	a) extinction/	Chemiluminescence will be monitored
	12		15 cm/s	lifted	to determine the lift-off height and
	13		20 cm/s		extinction limit.
	14		25 cm/s		Tests may be removed from (or added
	15		30 cm/s		to) this run based on the initial
	16		v(bo)-4 cm/s		exploratory test.
	17		v(bo)-3 cm/s		
	18		v(bo)-2 cm/s		
	19		v(bo)-1 cm/s		REQUIRED
	20		v(bo)-0.5 cm/s		
3	21	30% (70%)	10 cm/s	a) extinction/	Chemiluminescence will be monitored
	22		15 cm/s	lifted	to determine the lift-off height and
	23		20 cm/s		extinction limit.
	24		25 cm/s		Tests may be removed from (or added
	25		30 cm/s		to) this run based on the initial
	26		v(bo)-4 cm/s		exploratory test.
	27		v(bo)-3 cm/s		
	28		v(bo)-2 cm/s		
	29		v(bo)-1 cm/s		REQUIRED
	30		v(bo)-0.5 cm/s		
4	31	40% (60%)	15 cm/s	a) dilute/	Chemiluminescence will be monitored
	32		20 cm/s	lifted	to determine the lift-off height and
	33		25 cm/s		flame shape as a function of velocity.
	34		30 cm/s		Smaller velocity increments may be
	35		35 cm/s		added for the 40% (60%) flame.
	36	50% (50%)	20 cm/s		
	37		25 cm/s		
	38		30 cm/s		HIGHLY DESIRED
	39		35 cm/s		
5	40	60% (40%)	25 cm/s	a) moderate/	Chemiluminescence will be monitored
	41		30 cm/s	lifted	to determine the lift-off height and
	42		35 cm/s		flame shape as a function of velocity.
	43	65% (35%)	25 cm/s		
	44		30 cm/s		
	45		35 cm/s		
	46	70% (30%)	25 cm/s		
	47		30 cm/s		DESIRED
	48		35 cm/s		
6	49	80% (20%)	25 cm/s	b) sooting	The transition towards sooting will
	50		30 cm/s		be monitored as the fluid velocity is
	51		35 cm/s		increased and the dilution level
	52	90% (10%)	25 cm/s		decreased.
	53		30 cm/s		
	54		35 cm/s		
	55	100% (0%)	25 cm/s		
	56		30 cm/s		REQUIRED
	57		35 cm/s		

Table 8. Test matrix for ethylene.
Note: v(bo) is the velocity at blow off determined from exploratory tests

Run	Test #	% C_2H_4 (% N_2)	Flow Velocity	Test type	Comments
7	58	10% (90%)	10 cm/s	a) extinction/	Chemiluminescence will be monitored
	59		15 cm/s	lifted	to determine the lift-off height and
	60		20 cm/s		extinction limit.
	61		25 cm/s		Tests may be removed from (or added
	62		30 cm/s		to) this run based on the initial
	63		v(bo)-4 cm/s		exploratory test.
	64		v(bo)-3 cm/s		
	65		v(bo)-2 cm/s		
	66		v(bo)-1 cm/s		REQUIRED
	67		v(bo)-0.5 cm/s		
8	68	15% (85%)	10 cm/s	a) extinction/	Chemiluminescence will be monitored
	69		15 cm/s	lifted	to determine the lift-off height as a
	70		20 cm/s		function of velocity.
	71		25 cm/s		
	72		30 cm/s		
	73		v(bo)-4 cm/s		
	74		v(bo)-3 cm/s		
	75		v(bo)-2 cm/s		
	76		v(bo)-1 cm/s		REQUIRED
	77		v(bo)-0.5 cm/s		
9	78	20% (80%)	10 cm/s	a) dilute/	Chemiluminescence will be monitored
	79		15 cm/s	lifted	to determine the lift-off height as a
	80		20 cm/s		function of velocity.
	81		25 cm/s		
	82		30 cm/s		
	83		v(bo)-4 cm/s		
	84		v(bo)-3 cm/s		
	85		v(bo)-2 cm/s		
	86		v(bo)-1 cm/s		HIGHLY DESIRED
	87		v(bo)-0.5 cm/s		
10	88	30% (70%)	10 cm/s	a) moderate/	Chemiluminescence will be monitored
	89		15 cm/s	lifted	to determine the lift-off height and
	90		20 cm/s		flame shape as a function of velocity.
	91		25 cm/s		A portion of these tests may be
	92		30 cm/s		removed, if necessary, based on time
	93		35 cm/s		and gas restrictions.
	94	40% (60%)	10 cm/s		
	95		15 cm/s		
	96		20 cm/s		
	97		25 cm/s		
	98		30 cm/s		DESIRED
	99		35 cm/s		
11	100	50% (50%)	10 cm/s	b) sooting	The transition towards sooting will
	101		15 cm/s		be monitored as the fluid velocity is
	102		20 cm/s		increased and the dilution level
	103		25 cm/s		decreased.
	104		30 cm/s		
	105		35 cm/s		
	106	50% (50%)	10 cm/s		
	107	(double-velocity	15 cm/s		
	108	fuel flow)*	20 cm/s		
	109		25 cm/s		
	110		30 cm/s		REQUIRED
	111		35 cm/s		

* In Run 11, Test #'s 106-111 above, the flow velocity of the fuel and inert are doubled to twice the value listed in the "Flow Velocity" column. The coflow is still run at the velocity listed.

3.4 Success Criteria

Success of the Coflow Laminar Diffusion Flame experiment will be judged on meeting the stated experimental objectives (Section 2.3) by acquiring results that lead to the stated data end products (SDEP, Section 2.5). Three different levels of success – minimal, significant, and complete success – are defined. An additional level of success is defined as satisfying our overall project goals (laid out in Section 2.1), which is not required for complete experimental success.

3.4.1 Minimum Success

Minimum success is defined to mean acquisition of sufficient scientific data from the experiment to perform a direct comparison with the numerical computations and publish at least one journal article. This minimal level of success may be achieved by obtaining basic information about the flame characteristics from the color images or UV images, possibly for a subset of the flame conditions outlined above. Meaningful subsets of the data might include data from a single fuel (methane or ethylene, but not both) or from either weak or sooting flames, but not both. Data would remain valuable for comparisons with computational models, albeit not as complete as would be desirable. For example, minimal success might come from obtaining data as follows:

1. Color images of nonsooting flames only (SDEP A1).
2. UV images of *OH** (and *CH**, desired) luminosity from nonsooting flames (towards SDEP A2).

This would provide data that would allow us to determine several of our science data end products including the following:

- Observation of lift-off heights as a function of dilution level (SDEP A4).
- Observation of extinction limits as a function of dilution level (SDEP A6).
- Observation of flame shape and size (SDEP A5).
- 2D images of *OH** (and *CH**, desired) concentrations (SDEP A2).
- Peak concentrations of *OH** (and *CH**, desired) as a function of fuel dilution (SDEP A3).

Similar “minimal success” subsets of data could be defined for sooting flames only, or datasets from one fuel only. In any of these cases, a paper could still be published on the limited results and their comparison to the computations.

3.4.2 High Success

High success is defined to mean acquisition of sufficient scientific data from the experiment to perform a direct comparison with the numerical computations and publish several journal articles. In addition to the information obtained for a minimal level of success, a significant level of success may be achieved by obtaining more detailed information about the flame characteristics from UV images for species concentrations and from soot diagnostics for soot volume fraction (for example):

1. 2D images of soot laser extinction and associated reference images
2. 2D images of multi-color soot luminosity (from pyrometry data).

This would provide data that would allow us to determine several of our science data end products including the following:

- 2D images of soot volume fraction (SDEP B11).
- 2D images of soot temperatures (SDEP B9).

3.4.3 Complete Success

Complete success is defined to mean acquisition of all data related to the experimental objectives. In addition to the information obtained for a significant level of success, a complete level of success may be achieved by obtaining complete information about the flame characteristics using the available diagnostic techniques, including full information on temperatures, extinction and sooting tendencies across the full range of flow conditions:

1. Multi-color images of TFP data, including reference images.
2. Images of soot extinction representing the peak soot volume fraction, including reference images.
3. Soot luminosity images representing the peak soot temperature, including reference images.

This would provide data that would allow us to determine several of our science data end products including the following:

- Radial temperature profiles from TFP (SDEP A7 and B8).
- Combined temperature fields from soot pyrometry and TFP (SDEP A7 and B8 with B9).
- Peak soot volume fraction as a function of fuel dilution over the full range of flow velocities (SDEP B12).

- Peak temperature as a function of fuel dilution over the full range of flow velocities (SDEP A8 and B10).

3.4.4 Additional Project Goals

The experiments will be deemed successful if data are obtained that are sufficient to characterize coflow laminar diffusion flames of methane and ethylene under high-quality, long duration microgravity conditions. Of particular interest will be stable flames at the extremes of the fuel dilution spectrum, namely weak, highly-lifted flames near extinction as well as pure or moderately diluted sooting flames. The data set acquired will be used to verify and improve the numerical computations through comparison of trends for lift-off heights, extinction limits, species concentrations, flame temperatures and sooting tendencies for the range of dilute flames and sooting flames. The overall project will be considered a success if the information gained from the flight experiments can be used to generate efficient and effective computational techniques with modified chemical kinetics mechanisms (Goal 1), and to develop refined submodels for soot formation (Goal 2) under normal and microgravity conditions for both methane and ethylene flames.

3.5 Post-flight Data Analysis Plan

Once data has been acquired on the ISS, it will need to be analyzed and compared with the computational results. As a first step, color flame images will be compared with simulated flame images from the computations (as discussed in Section 2.7). From this comparison we will be able to determine if the computations capture the overall changes that occur over the range of flow conditions as the flame is moved from normal gravity to microgravity. This relatively simple diagnostic technique can provide information on lift-off height, overall flame shape, sooting tendencies, and extinction limits. These results can begin to provide feedback for the computational model's effectiveness in modeling flame phenomena at microgravity.

Data collected from chemiluminescence will then be analyzed. Data are acquired as a line-of-sight projection, so a tomographic inversion, such as an Abel inversion [42, 43], will be used to determine radial profiles of OH^* and/or CH^*. If pre-flight spectral calibration data are available for the UV camera, quantitative number densities can be determined. However, even without calibration, the relative chemiluminescence profiles can be used to infer information about extinction limits and lift-off height as a function of fuel dilution and flow velocity. This

information determined in μg will be compared to results at normal gravity and to results from the computations.

Images of the blackbody radiation from the soot are also taken along a line-of-sight at two or more wavelengths. Each separate color image must be tomographically inverted and the resulting radial profiles from the soot pyrometry data used to determine the local soot temperature using color signal ratios under the two-color method. These resulting temperatures will be combined with the intensity distribution of a single color image to determine the soot volume fraction. This μg data will be compared to data taken at 1 g to determine the relative variation in peak temperatures and increase in sooting across all flow conditions investigated. The results can then be used in comparison with the numerically determined soot temperatures and soot volume fractions.

Images of TFP data will be analyzed using two-color pyrometry. Each radial image pair of the filament will be processed using the two-color method to determine temperatures along a line at a specific height above the burner. Data taken at multiple heights will be composed into a two-dimensional image for each flame condition. The TFP data can then be combined with the soot pyrometry data (for the flames containing soot) in order to create more complete temperature fields. The combined data will be used to determine peak temperatures across the range of cases studied.

The primary determination of soot volume fractions will come from the laser extinction measurements. Two images of laser transmission are taken for each flame case: one with the flame and one without. Taking the ratio of the intensity of the beam transmitted through the flame to the intensity of the beam without the flame will be used to determine the integrated optical thickness of soot within the flame using the Lambert-Beer law. The radial profile of the optical thickness will be determined by performing a tomographic inversion on the integrated signal. The soot volume fraction will then be calculated by applying values for the extinction coefficient of soot at the laser wavelength and the characteristic length of the flame at each location. Finally, the soot temperatures can be determined using the optical thickness field with the appropriate physical constants and blackbody spectrum at the laser wavelength. The soot volume fraction and temperature will be determined for all cases studied, and the results can be compared to the pyrometry data where there is overlapping data.

Data from all measurement techniques will be combined to provide as complete information as possible for each flame over the range of flow conditions studied. These results will be compared to the numerical simulations for each case, and for trends across various flow conditions. Modifications may then be made to improve the model based on these comparisons.

The largest source of error in a majority of techniques used to determine sooting characteristics relates to the optical properties of the soot. The values of the soot absorption function, *E(m)*, and the dimensionless extinction coefficient, K_{ext}, have been the subject of numerous investigations [44-46], and are known to vary by as much as 20%. Both quantities are difficult to determine partially because they are a function of the particular soot properties (e.g., primary particle size, aggregate size), which vary with the fuel used and the exact location within each flame. Indeed microgravity effects on the optical properties of soot represent another source of uncertainty, with larger aggregates of different fractal dimension having been observed under microgravity conditions [47]. The model of light scattering used in each determination of *E(m)* and K_{ext} can also vary. In the Rayleigh approximation of small particles K_{ext} is dominated by absorption. As the soot particles aggregate into larger structures, this approximation is no longer valid and the soot must be considered as fractal aggregates. Since it is impractical to independently measure K_{ext} for all flame cross sections, an average value (e.g., K_{ext}=8.6 [45]) will be used to determine the soot volume fraction using both pyrometry and extinction, and in the determination of the radiation field in the numerical computations. Clearly, this constant value of K_{ext} is not entirely accurate, particularly near the burner exit, but it is at the very least consistent across all determinations of sooting characteristics, which should allow for comparison of trends within each flame and across the various flow conditions. Given the increase in residence time under microgravity conditions, the optical properties of the soot are expected to vary even more as the increase in total particles is expected to cause higher levels of aggregation and potentially agglomeration.

4 REFERENCES

1. Bahadori, M.Y., Edelman, R.B., Stocker, D.P., and Olson, S.L., *Ignition and Behavior of Laminar Gas-Jet Diffusion Flames in Microgravity.* AIAA Journal, 1990. **28**(2): p. 236-244.
2. Hegde, U., Bahadori, M.Y., and Stocker, D.P., *Oscillatory temperature measurements in a pulsed microgravity diffusion flame.* AIAA Journal, 2000. **38**(7): p. 1219-1229.
3. Sunderland, P.B., Mendelson, B.J., Yuan, Z.G., and Urban, D.L., *Shapes of buoyant and nonbuoyant laminar jet diffusion flames.* Combustion and Flame, 1999. **116**(3): p. 376-386.
4. Hermanson, J.C., Johari, H., Stocker, D.P., and Hegde, U.G., *Buoyancy effects in strongly pulsed turbulent diffusion flames.* Combustion and Flame, 2004. **139**(1-2): p. 61-76.
5. Aalburg, C., Diez, F.J., Faeth, G.M., Sunderland, P.B., Urban, D.L., and Yuan, Z.G., *Shapes of nonbuoyant round hydrocarbon-fueled laminar-jet diffusion flames in still air.* Combustion and Flame, 2005. **142**(1-2): p. 1-16.
6. Briones, A.M., Aggarwal, S.K., and Katta, V.R., *A numerical investigation of flame liftoff, stabilization, and blowout.* Physics of Fluids, 2006. **18**(4).
7. Datta, A., *Effects of gravity on structure and entropy generation of confined laminar diffusion flames.* International Journal of Thermal Sciences, 2005. **44**(5): p. 429-440.
8. Vietoris, T., Joulain, P., and Torero, J.L., *Experimental characterization of a laminar diffusion flame in micro-gravity.* Journal De Chimie Physique Et De Physico-Chimie Biologique, 1999. **96**(6): p. 1022-1030.
9. Lin, K.C., Faeth, G.M., Sunderland, P.B., Urban, D.L., and Yuan, Z.G., *Shapes of nonbuoyant round luminous hydrocarbon/air laminar jet diffusion flames.* Combustion and Flame, 1999. **116**(3): p. 415-431.
10. Takahashi, F. and Katta, V.R., *Reaction kernel structure and stabilizing mechanisms of jet diffusion flames in microgravity.* Proceedings of the Combustion Institute, 2003. **29**: p. 2509-2518.
11. Takahashi, F. and Katta, V.R., *Further studies of the reaction kernel structure and stabilization of jet diffusion flames.* Proceedings of the Combustion Institute, 2005. **30**: p. 383-390.
12. Walsh, K.T., Fielding, J., Smooke, M.D., Long, M.B., and Linan, A., *A comparison of computational and experimental lift-off heights of coflow laminar diffusion flames.* Proceedings of the Combustion Institute, 2005. **30**: p. 357-365.
13. Bahadori, M.Y., Stocker, D.P., Zhou, L., and Hegde, U., *Radiative loss from non-premixed flames in reduced-gravity environments.* Combustion Science and Technology, 2001. **167**: p. 169-186.
14. Walsh, K.T., Fielding, J., Smooke, M.D., and Long, M.B., *Experimental and computational study of temperature, species, and soot in buoyant and non-buoyant coflow laminar diffusion flames.* Proceedings of the Combustion Institute, 2000. **28**: p. 1973-1979.
15. Fuentes, A., Rouvreau, S., Joulain, P., Vantelon, J.P., Legros, G., Torero, J.L., and Fernandez-Pello, A.C., *Sooting behavior dynamics of a non-buoyant laminar diffusion flame.* Combustion Science and Technology, 2007. **179**(1-2): p. 3-19.

16. Fujita, O. and Ito, K., *Observation of soot agglomeration process with aid of thermophoretic force in a microgravity jet diffusion flame.* Experimental Thermal and Fluid Science, 2002. **26**(2-4): p. 305-311.
17. Sunderland, P.B., Urban, D.L., Stocker, D.P., Chao, B.H., and Axelbaum, R.L., *Sooting limits of microgravity spherical diffusion flames in oxygen-enriched air and diluted fuel.* Combustion Science and Technology, 2004. **176**(12): p. 2143-2164.
18. Idicheria, C.A., Boxx, I.G., and Clemens, N.T., *Characteristics of turbulent nonpremixed jet flames under normal- and low-gravity conditions.* Combustion and Flame, 2004. **138**(4): p. 384-400.
19. Legros, G., Joulain, P., Vantelon, J.P., and Fuentes, A., *Soot volume fraction measurements in a three-dimensional laminar diffusion flame established in microgravity.* Combustion Science and Technology, 2006. **178**(5): p. 813-835.
20. Ezekoye, O.A. and Zhang, Z., *Convective and radiative coupling in a burner-supported diffusion flame.* Journal of Thermophysics and Heat Transfer, 1997. **11**(2): p. 239-245.
21. Ezekoye, O.A. and Zhang, Z., *Soot oxidation and agglomeration modeling in a microgravity diffusion flame.* Combustion and Flame, 1997. **110**(1-2): p. 127-139.
22. Lock, A.J., Briones, A.M., Qin, X., Aggarwal, S.K., Puri, I.K., and Hegde, U., *Liftoff characteristics of partially premixed flames under normal and microgravity conditions.* Combustion and Flame, 2005. **143**(3): p. 159-173.
23. Qin, X., Puri, I.K., Aggarwal, S.K., and Katta, V.R., *Gravity, radiation, and coflow effects on partially premixed flames.* Physics of Fluids, 2004. **16**(8): p. 2963-2974.
24. Rouvreau, S., Joulain, P., Wang, H.Y., Cordeiro, P., and Torero, J.L., *Numerical evaluation of boundary-layer assumptions used for the prediction of the standoff distance of a laminar diffusion flame.* Proceedings of the Combustion Institute, 2003. **29**: p. 2527-2534.
25. Urban, D.L., Yuan, Z.G., Sunderland, P.B., Lin, K.C., Dai, Z., and Faeth, G.M., *Smoke-point properties of non-buoyant round laminar jet diffusion flames.* Proceedings of the Combustion Institute, 2000. **28**: p. 1965-1972.
26. Urban, D.L., Yuan, Z.G., Sunderland, P.B., Linteris, G.T., Voss, J.E., Lin, K.C., Dai, Z., Sun, K., and Faeth, G.M., *Structure and soot properties of nonbuoyant ethylene/air laminar jet diffusion flames.* AIAA Journal, 1998. **36**(8): p. 1346-1360.
27. Xu, F., Dai, Z., and Faeth, G.M., *Flame and soot boundaries of laminar jet diffusion flames.* AIAA Journal, 2002. **40**(12): p. 2439-2446.
28. Faeth, G.M., *Laminar and Turbulent Gaseous Diffusion Flames*, in *Microgravity Combustion*, H.D. Ross, Editor. 2001, Academic Press: London. p. 83-182.
29. Walsh, K.T., Fielding, J., and Long, M.B., *Effect of light-collection geometry on reconstruction errors in Abel inversions.* Optics Letters, 2000. **25**(7): p. 457-459.
30. Walsh, K.T., Long, M.B., Tanoff, M.A., and Smooke, M.D., *Experimental and computational study of CH, CH*, and OH* in an axisymmetric laminar diffusion flame.* Proceedings of the Combustion Institute, 1998. **27**(Vol. 1): p. 615-623.
31. Luque, J., Jeffries, J.B., Smith, G.P., Crosley, D.R., Walsh, K.T., Long, M.B., and Smooke, M.D., *CH(A-X) and OH(A-X) optical emission in an axisymmetric laminar diffusion flame.* Combustion and Flame, 2000. **122**(1/2): p. 172-175.
32. Walsh, K.T., *Quantitative Characterizations of Coflow Laminar Diffusion Flames in a Normal Gravity and Microgravity Environment*. 2000, Yale University.

33. Kuhn, P.B., Ma, B., Connelly, B.C., Smooke, M.D., and Long, M.B., *Soot and Thin-filament Pyrometry Using a Color Digital Camera.* Proceedings of the Combustion Institute, 2010. **33**.
34. Levendis, Y.A., Estrada, K.R., and Hottel, H.C., *Development of Multicolor Pyrometers to Monitor the Transient-Response of Burning Carbonaceous Particles.* Review of Scientific Instruments, 1992. **63**(7): p. 3608-3622.
35. Snelling, D.R., Thomson, K.A., Smallwood, G.J., Gulder, O.L., Weckman, E.J., and Fraser, R.A., *Spectrally resolved measurement of flame radiation to determine soot temperature and concentration.* AIAA JOURNAL, 2002. **40**(9): p. 1789-1795.
36. Dietrich, D. and Ross, H. *Candle Flames in Microgravity Home Page*. 2007 [cited 2007; Available from: http://microgravity.grc.nasa.gov/combustion/cfm/cfm_index.htm
37. Stocker, D.P., *Personal Communication*. 2007.
38. Hall, R.J., Smooke, M.D., and Colket, M.B., *Predictions of soot dynamics in opposed jet diffusion flames.* Combustion Science and Technology Book Series, 1997. **4**(Physical and Chemical Aspects of Combustion): p. 189-230.
39. Sun, C.J., Sung, C.J., Wang, H., and Law, C.K., *On the structure of nonsooting counterflow ethylene and acetylene diffusion flames.* Combustion and Flame, 1996. **107**(4): p. 321-335.
40. Smooke, M.D., Hall, R.J., Colket, M.B., Fielding, J., Long, M.B., McEnally, C.S., and Pfefferle, L.D., *Investigation of the transition from lightly sooting towards heavily sooting co-flow ethylene diffusion flames.* Combustion Theory and Modelling, 2004. **8**(3): p. 593-606.
41. Cignoli, F., De Iuliis, S., Manta, V., and Zizak, G., *Two-dimensional two-wavelength emission technique for soot diagnostics.* Applied Optics, 2001. **40**(30): p. 5370-5378.
42. Dasch, C.J., *One-Dimensional Tomography - a Comparison of Abel, Onion-Peeling, and Filtered Backprojection Methods.* Applied Optics, 1992. **31**(8): p. 1146-1152.
43. Walsh, K.T., Fielding, J., and Long, M.B., *Effect of Light Collection Geometry on Reconstruction Errors in Abel Inversions.* Opt. Lett., 2000. **25**: p. 457.
44. Krishnan, S.S., Lin, K.C., and Faeth, G.M., *Optical properties in the visible of overfire soot in large buoyant turbulent diffusion flames.* Journal of Heat Transfer-Transactions of the Asme, 2000. **122**(3): p. 517-524.
45. Krishnan, S.S., Lin, K.C., and Faeth, G.M., *Extinction and scattering properties of soot emitted from buoyant turbulent diffusion flames.* Journal of Heat Transfer-Transactions of the Asme, 2001. **123**(2): p. 331-339.
46. Williams, T.C., Shaddix, C.R., Jensen, K.A., and Suo-Anttila, J.M. *Measurement of the Dimensionless Extinction Coefficient of Soot within Laminar Diffusion Flames*. in *Joint Meeting of the U.S. Sections of the Combustion Institute*. 2005.
47. Ku, J.C., Griffin, D.W., Greenberg, P.S., and Roma, J., *Buoyancy-Induced Differences in Soot Morphology.* Combustion and Flame, 1995. **102**: p. 216 - 218.
48. Snelling, D.R., Liu, F.S., Smallwood, G.J., and Gulder, O.L., *Determination of the soot absorption function and thermal accommodation coefficient using low-fluence LII in a laminar coflow ethylene diffusion flame.* Combustion and Flame, 2004. **136**(1-2): p. 180-190.
49. Zhu, J.Y., Irrera, A., Choi, M.Y., Mulholland, G.W., Suo-Anttila, J., and Gritzo, L.A., *Measurement of light extinction constant of JP-8 soot in the visible and near-infrared*

spectrum. International Journal of Heat and Mass Transfer, 2004. **47**(17-18): p. 3643-3648.
50. Daun, K.J., Thomson, K.A., Liu, F.S., and Smallwood, G.J., *Deconvolution of axisymmetric flame properties using Tikhonov regularization.* Applied Optics, 2006. **45**(19): p. 4638-4646.

5 APPENDICES

5.1 APPENDIX A: Laser-Based Microgravity Measurements Aboard The KC-135

For our laser-based μg measurements, a third rack containing a compact, high-power pulsed Nd:YAG laser (Big Sky CFR 400), was added to the experimental equipment described earlier. This laser produces up to 220 mJ per pulse in the green (at 532 nm) and operates at 10 Hz. The 532 nm beam was shaped, steered through a window, and brought to a focus over the burner centerline. Other additions included an image intensifier and associated timing electronics, a stepper motor for the burner, and a three-axis accelerometer mounted directly to the experiment rack to provide a measure of local gravitational fluctuations.

For Rayleigh thermometry measurements, the beam was shaped into a 12 mm tall sheet with moderate laser power (80 mJ/pulse). These measurements were performed single-shot at flow conditions of interest to assess flame stability. Once the stability of the single-shot flame images was confirmed, 100-shot integrated measurements were made in the flame as well as in uniform concentrations of air and helium to produce background and response-corrected images. The variation of the Rayleigh cross section in the flame is accounted for in an iterative procedure. This procedure converges quickly, producing two-dimensional temperature measurements.

The first measurement of these flames focused on the “standard” flow conditions, 65/35, to investigate the role of buoyancy in this extensively characterized flame. Measured and computed temperature distributions in the 65/35 flame are directly compared in Fig. A1. Excellent agreement in flame structure and lift-off height can be seen in the normal gravity flame. In the μg flame, we see the computations successfully predict that when the influence of gravity is removed, the high temperature zone becomes shorter and wider. The measured and predicted centerline temperature profiles, not shown, reveal good agreement in peak temperature in 1g, although the flame length is somewhat over-predicted. Agreement in the nonbuoyant flame is excellent – flame lift-off, lower peak temperature, and shorter flame length are all well predicted.

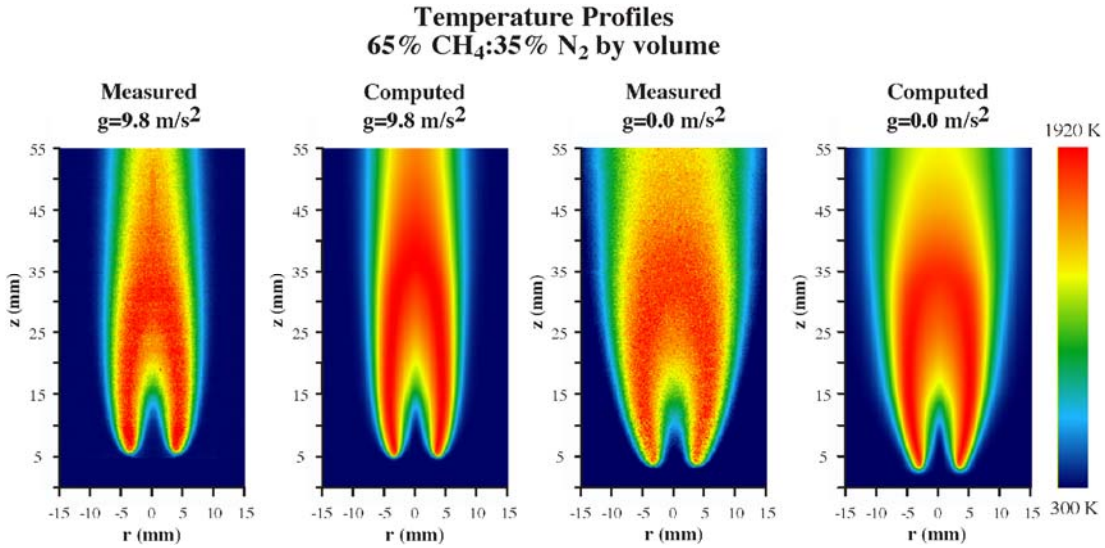

Fig. A1. Measured and computed temperature profiles at standard flow conditions.

As nitrogen is added to the fuel stream in 5% increments (by volume), the normal gravity blow-off limit is reached for dilution levels beyond the 40/60 flow condition. Temperature fields were measured and computed at this experimental limit, as can be seen in Fig. A2. The normal gravity flame is highly lifted, in strong disagreement with computational prediction. This discrepancy exists to a lesser extent in the μg flame. In both normal gravity and μg, the computed peak centerline temperature is higher than measurement by 40 K, which is within measurement error. While mixtures more dilute than 40/60 cannot be stabilized in normal gravity, flames with fuel mixtures as dilute as 30/70 were possible aboard the KC-135. Temperature distributions were measured for both the 35/65 and 30/70 flames. Though the 35/65 flame was stable, the 30/70 flame moved 1 to 2 mm during a given low-g maneuver. This flame is extremely flat, faint, and highly lifted, anchoring roughly 37 mm above the burner surface.

Raman measurements of fuel and oxygen were performed with the laser at full power (220 mJ/pulse), focused down to a line with 300 μm beam waist. The Raman signal was integrated over 100 shots along the laser line in two distinct spectral regions at separate times. The first measurements used a 630 nm center, 10 nm bandpass filter to measure methane Raman scattering. The second set utilized a 590 nm center, 10 nm bandpass filter to measure Raman scattering from oxygen. The 10 nm spectral region centered on the oxygen Raman peak also includes a significant interference from methane Raman scattering. After measurements are made in both spectral regions, the appropriately scaled methane measurement can be subtracted

from the (O_2+CH_4) measurement to result in a measured oxygen profile. These measurements produce quantitative O_2 and CH_4 number density profiles.

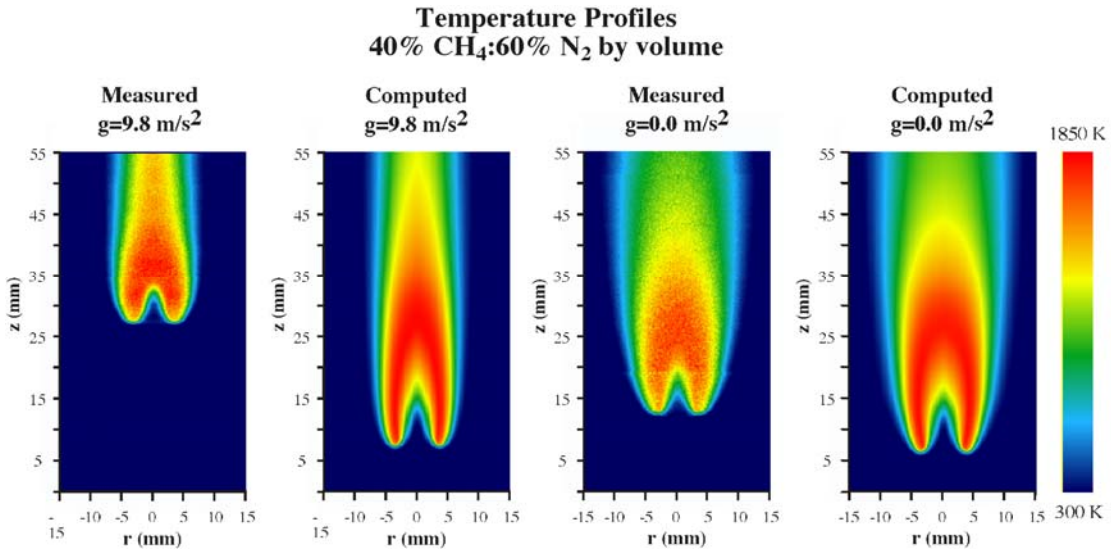

Fig. A2. Measured and computed temperature profiles at the normal gravity blow-off limit.

Fuel and oxygen Raman measurements were performed in both μg and normal gravity at the 65/35 and 40/60 flow conditions. These conditions were chosen to study air/fuel mixing in a flame that is well predicted (65/35) and in a dilute flame where the computational model has less predictive ability. The predicted and measured oxygen profiles are shown for the 65/35 flame in Fig. A3. In the measured normal gravity image, a left-right flame asymmetry can be seen – the flame anchors in a slightly different location on either side of the jet centerline, while the computations assume perfect cylindrical symmetry. In comparing measured and computed O_2 profiles, the characteristics of the "horn-like" structure of air being entrained into the fuel stream are of particular interest. At this "standard" flow condition in normal gravity, this structure compares well on one side but not the other. On the right side of the measured flame is a plume of oxygen that is more concentrated and extends further downstream than any predicted by the computation. In μg, however, the measured flame is extremely symmetric, with the behavior at the fuel/oxygen interface well predicted by computation. Note that in both measured oxygen images, a fluorescence interference can be seen in the O_2-free "hot zone" region.

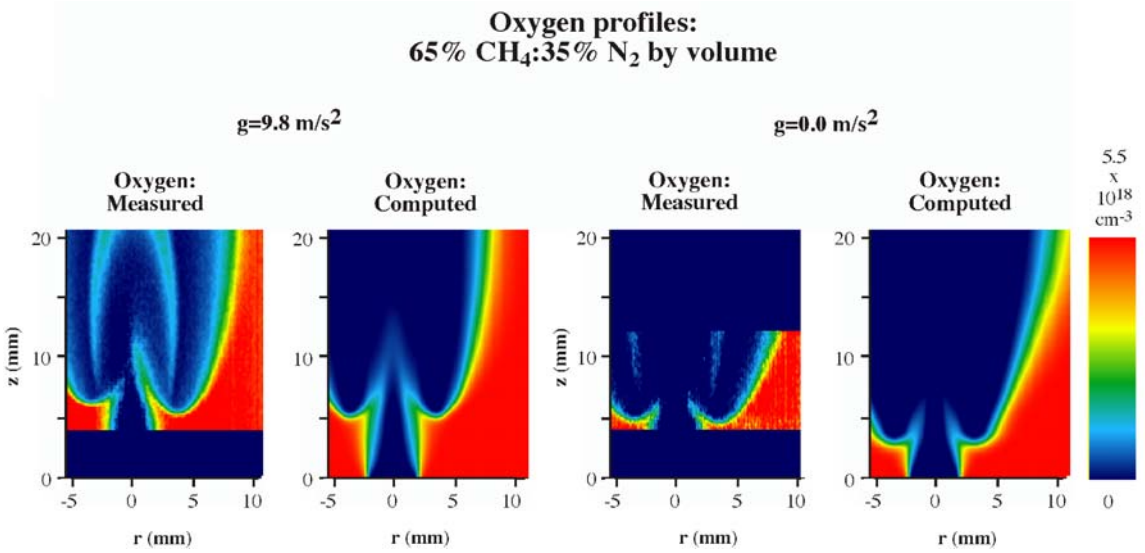

Fig. A3. Measured and computed oxygen profiles at standard flow conditions.

Laser-induced incandescence (LII) measurements were made with the laser shaped into a 15 mm sheet for maximum spatial coverage. A blue-additive filter, which transmitted roughly 90% between 400 nm and 450 nm, was used in the detection system. For all sooting flames studied in normal gravity and microgravity, the LII signal was measured as a function of laser intensity to ascertain an optimum per pulse energy for the determination of soot volume fraction. Since the soot field was observed to fluctuate during "g-jitter" on the KC-135, the LII images taken in µg are single-shot. These time-resolved images are indexed with the local acceleration to assess the behavior of these flames in an unsteady gravitational field. Flame luminosity background measurements were made in µg but could not be subtracted from measured LII signals due to the unsteadiness present in the flames. Single-shot LII measurements were made successfully in the 100% CH_4 (100/0) flame, where five measurements can be made during a given low-g parabola. For normal gravity measurements, the soot levels present in methane flames were insufficient to allow for single-shot measurements, so a 100-shot integration was used.

In making laser-induced incandescence (LII) measurements on the KC-135, single-shot measurements were repeated at multiple times to assess the fluctuations in soot volume fraction and distribution in relation to the time-varying local acceleration. In a given 15 mm region above the burner surface, the peak soot volume fraction can vary by as much as 50% over the course of a low-g parabola. However, the measured soot concentration and distribution is repeatable for

measurements made during similar g-levels and g-histories. Therefore, the distribution which results after a long (>3 s) period of "g = 0" is considered to be the best available soot measurement in the noisy gravitational field available aboard the KC-135. The measured soot distribution in normal gravity and this best available μg measurement are shown together in Fig. A4. When the influence of gravity is removed, the (uncalibrated) peak soot volume fraction increases by a factor of 15 while the soot-containing region contracts axially and expands radially. It should be noted, however, that in making the LII measurements, a relatively long gate time was used on the image intensifier. This increases the detected signal, but tends to emphasize the contributions from larger particles. Since it has been shown that soot aggregates are larger in microgravity, the increase in soot volume fraction may not be as great as indicated by the difference in LII intensity.

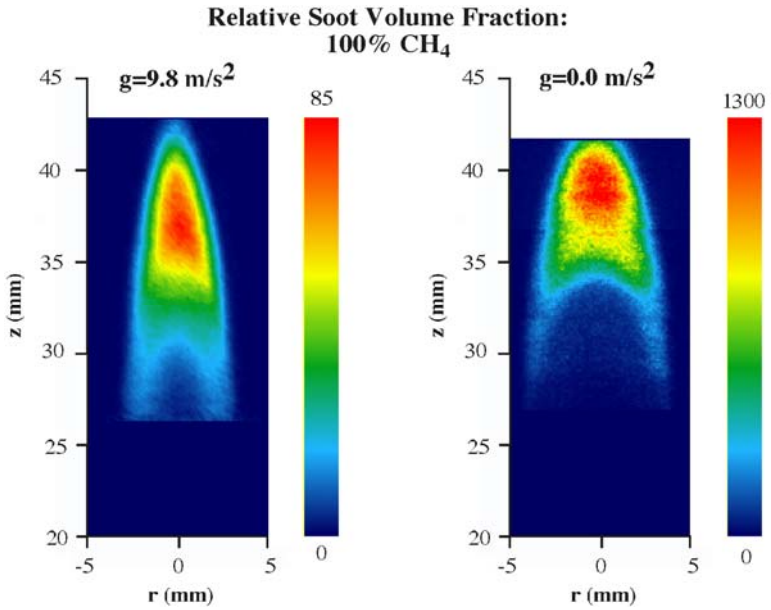

Fig. A4. Measured soot profiles in the 100/0 flame.

5.2 APPENDIX B: Analysis of the Pressurization of a Sealed Experimental Chamber

Since active venting of the Combustion Integrated Rack (CIR) will not be possible, the effect of operating our coflow burner in a closed chamber must be considered. As a first attempt to minimize pressure increases in the sealed experimental chamber, the planned size of the coflow burner was reduced to minimize pressure increases within the vessel by using as low flow rates as possible and thus increase the amount of time the experiment can run while sealed. However, even with the reduced flow rates achieved by decreasing the burner diameter, significant increases in pressure in the vessel are expected. The following discussion details the calculations used to determine the expected increase in chamber pressure.

Modeling the gas within the chamber as an ideal gas, increases to the chamber pressure can be calculated by including the increase in mass in the chamber due to gas flow out of the burner and increase in chamber temperature due to flame heating. A constant mass flow rate has been used instead of a constant volumetric flow rate because the mass flow controllers provide a constant mass flow and the increased pressure is expected to affect volumetric flow rates. The mass flow rates were determined using our standard volumetric flow rates, which were calibrated at standard ambient temperature and pressure (SATP) conditions (300 K, 1.01325 bar).

The time rate of change of the pressure in the chamber can be determined by taking the time derivative of the ideal gas law

$$\frac{dP}{dt} = \frac{RT}{W_{air}V_{cyl}}\dot{m} + \frac{R}{W_{air}V_{cyl}}m_{air}\frac{dT}{dt} \qquad \text{(B1)}$$

where P is the chamber pressure, R is the ideal gas constant, T is the gas temperature in the chamber, W_{air} is the molecular weight of air, V_{cyl} is the volume of the chamber (assumed to be 80 liters here), and $\dot{m}$ is the mass flow rate into the chamber (a constant). Variables in Eq. B1 are T and m_{air}, and must be determined by considering the heating of the chamber from the flame. The mass as a function of time can easily be determined using the initial mass within the chamber at SATP and introducing mass at a rate of $\dot{m}$. For all cases a mixture of 50% C_2H_4 and 50% N_2 is assumed to undergo complete combustion, and the heat of combustion is calculated for varying flow rates exiting a 2.1 mm diameter tube. For example, a flow rate of 35 cm/s is

estimated to produce a flame that heats the chamber at a rate of $\dot{Q}$=65.2 J/s. The temperature can then be determine using

$$Q = m_{total} c_v \Delta T \tag{B2}$$

where Q is the heat added to the chamber, c_v is the specific heat (taken at constant volume for air), and m_{total} considers the total mass of the system included the chamber housing (assumed here to be aluminum). Taking the derivative of Eq. B2 yields

$$\dot{Q} = 65.2\, J/s = \left(m_{Al} c_{Al} + m_{air} c_{v,air}\right) \frac{d(\Delta T)}{dt} + \dot{m} c_{v,air} \Delta T \tag{B3}$$

where the product of the mass of the chamber housing and the specific heat of aluminum, $m_{Al} c_{Al}$, have now been included. Eqs. B1 and B3 can be solved iteratively to determine the temperature and pressure of the gas in the chamber. Initial ambient conditions are taken to be at SATP (300 K, 1.01325 bar). The resulting pressure is plotted as a function of time in Fig. B1 for six different initial flow velocities.

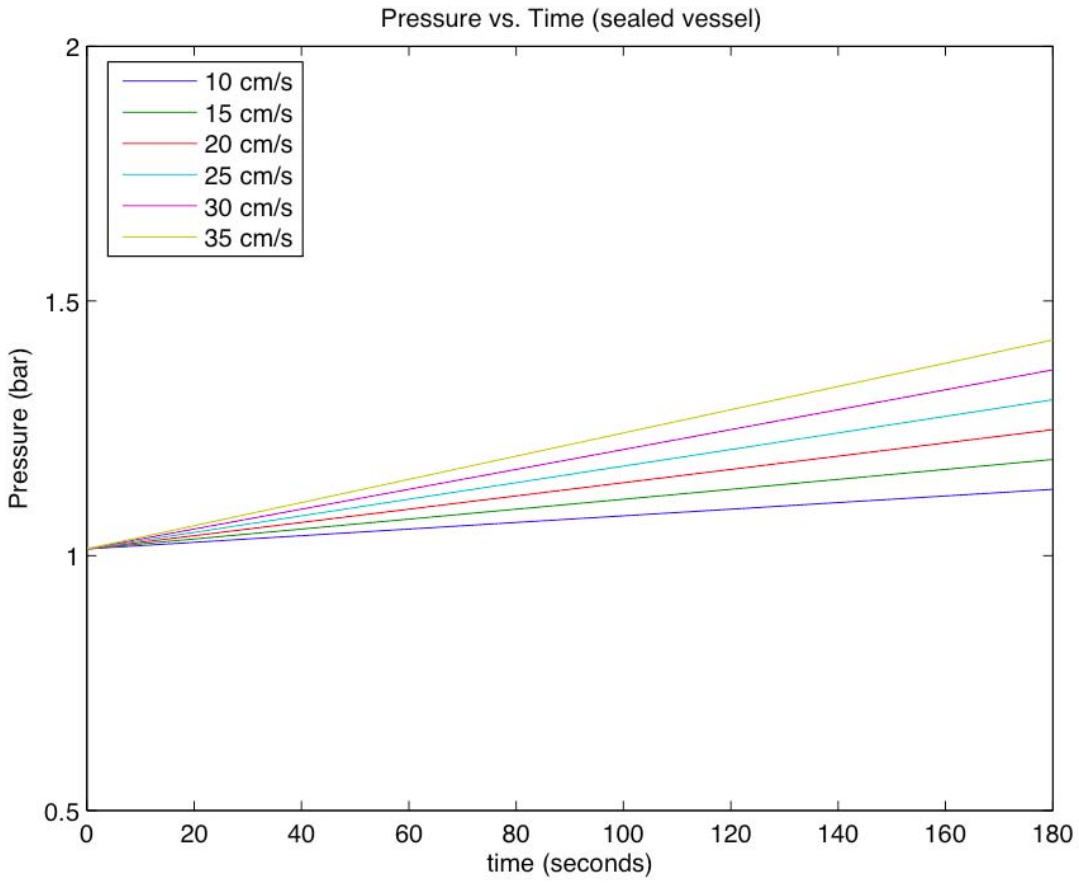

Fig. B1. Calculated chamber pressure plotted as a function of time. The average flow velocities at SATP are indicated for each case.

The pressure is found to increase at a rate of 0.137 bar/min, while the temperature is found to increase at a negligible rate of 0.2 K/min. The reason that the temperature effects are so small is due to the inclusion of the mass of the chamber in the control volume used to consider the heating from the flame. If the mass of the chamber were not included, the temperature would increase significantly faster, also increasing the pressure. The results of the pressure and temperature calculation are shown in Fig. B2 and B3, respectively, with the chamber mass both included and excluded for the 35 cm/s SATP case. Due to experimental observations (shown in Appendix C) we conclude that the mass of the chamber is important when considering flame heating effects.

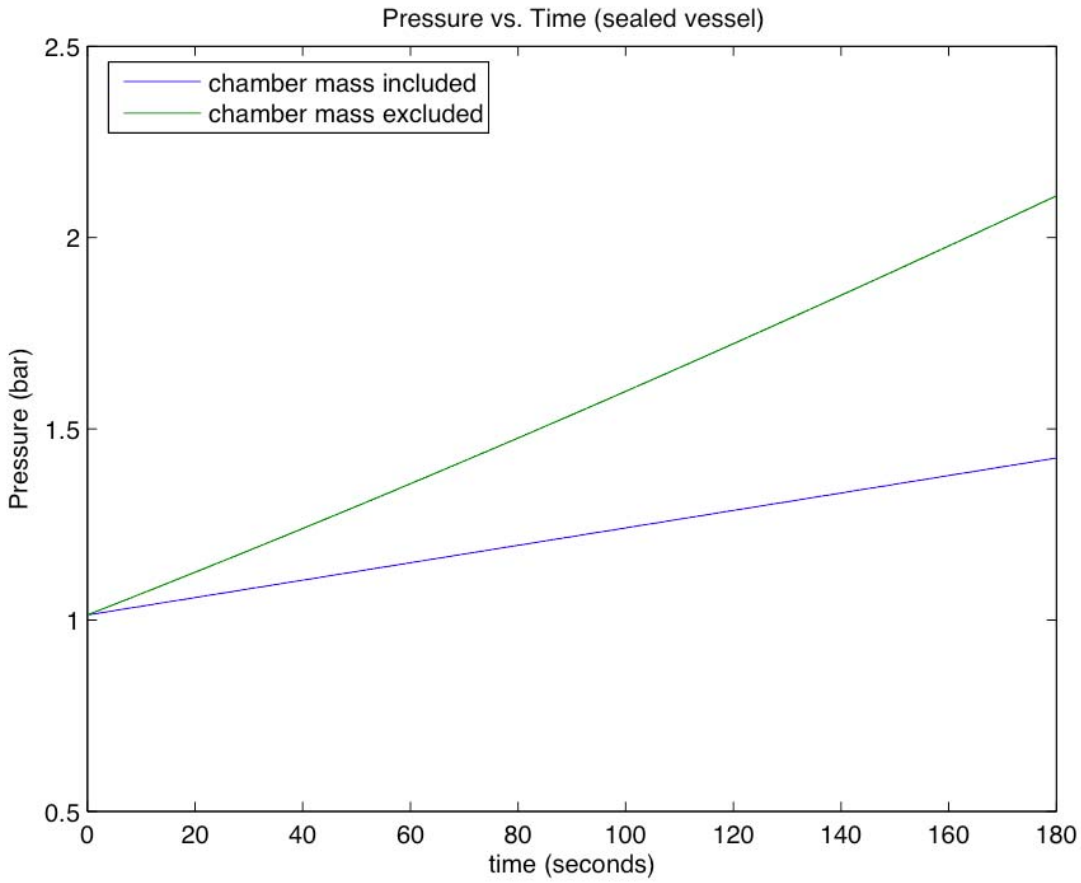

Fig. B2. Calculated chamber pressure plotted as a function of time. The average flow velocity is 35 cm/s at SATP for both traces. The blue line corresponds to including the chamber mass in the calculation, while the green line corresponds to excluding the chamber mass in the calculation.

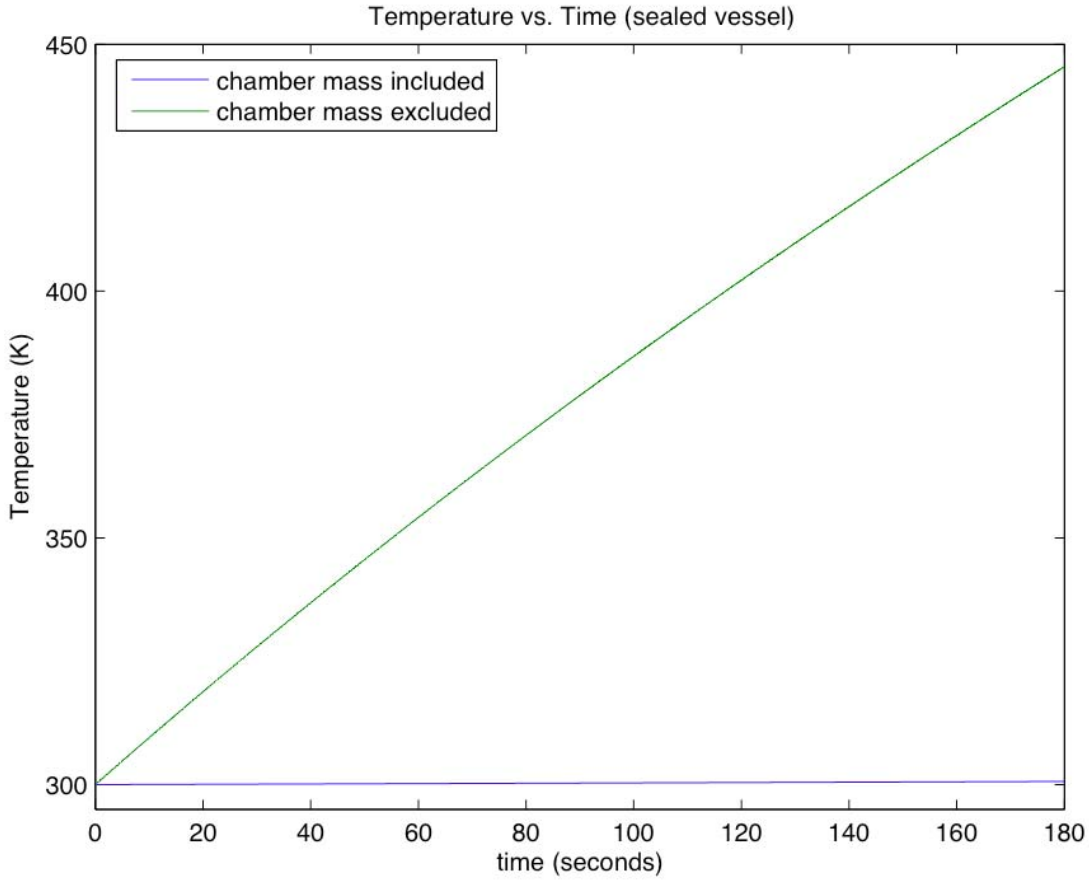

Fig. B3. Calculated chamber temperature plotted as a function of time. The average flow velocity is 35 cm/s at SATP for both traces. The blue line corresponds to including the chamber mass in the calculation, while the green line corresponds to excluding the chamber mass in the calculation.

Using the increased pressure and the constant mass flow rate, $\dot{m}$, the average exit velocity can be determined as a function of time. A plot of the exit velocity is provided in Fig. B4 for six different initial flow velocities. It can be seen that the 35 cm/s case experiences a decrease in flow velocity of approximately 5 cm/s over the course of a 3-minute run time.

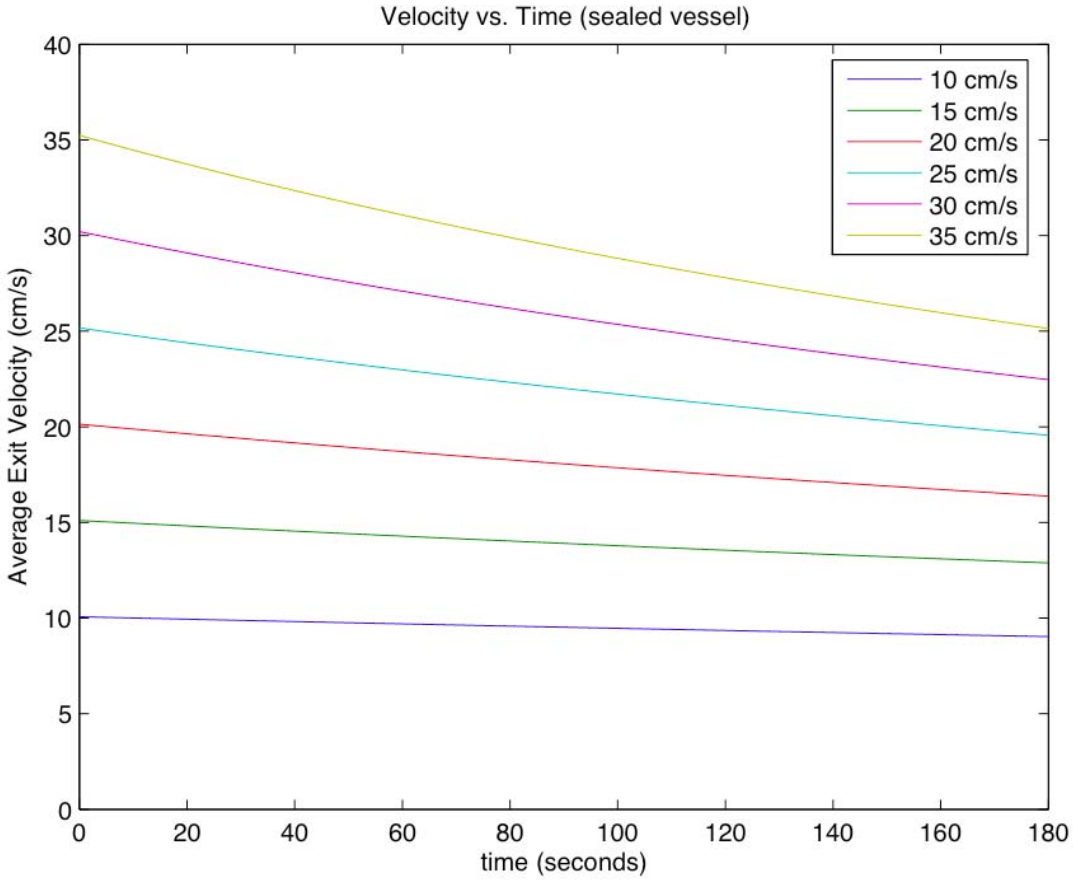

Fig. B4. Calculated exit velocity plotted as a function of time. The average flow velocities at SATP are indicated for each case.

5.3 APPENDIX C: Pyrometry Measurements of Sooting Flames

Soot emission measurements were made in a series of flames using three-color optical pyrometry with a color digital camera (the Nikon D70). Typical optical pyrometers use multiple detectors at different wavelengths, requiring proper alignment and calibration of each detector with respect to one another. The use of the built-in color filter array (CFA) of a digital camera allows for two-dimensional imaging of flame emission spectra at the wavelengths of the color filters, without the need to spatially match images taken at the different wavelengths. The raw image data provide pixel-by-pixel spectral and spatial information in the form of three separate images which are taken from a single camera shot by separating the red, green and blue channels. The two-dimensional flame temperatures can then be calculated using the two-color method [34]. Images were taken of an oven at varying temperatures, and the results were used to provide a blackbody calibration for the camera. Once local soot temperatures have been determined using the two-color method, the blackbody calibration makes it possible to calculate the soot volume fraction [41, 48, 49]. Previous experiments in a different set of flames have shown that resulting soot volume fractions agree well with measurements made using laser-induced incandescence (LII).

Observations of sooting flames inside a sealed chamber show that the brightness of the soot luminosity increases with increasing ambient pressure. Measurements were made with the digital camera in order to determine the soot temperatures and volume fractions as a function of time and ambient pressure for two cases of the 50% C_2H_4 / 50% N_2 flame: a 35 cm/s coflow and fuel flow velocity (denoted 35 cm/s), and a 35 cm/s coflow and 70 cm/s fuel flow velocity (denoted 70 cm/s). Images were acquired at 15-second intervals as the sealed chamber pressurized due to the inflow of gases from the burner and heating from the flame (negligible), beginning with standard atmospheric temperature and pressure conditions (1.01325 bar) at 0 seconds. The corresponding pressures, which were determined from an independent data run, are plotted in Fig. C1. The data points correspond to the times that flame images were taken. The line-of-sight images were separated into their red, green and blue components, and the radial profile of each separate color image was computed using an Abel inversion [29, 42, 50]. The radial profiles were then used to compute the soot temperatures using the two-color method, and the resulting temperatures were combined with the green channel's image to determine the soot volume fraction. For the calculations shown here, the dimensionless extinction coefficient is taken to be

10 [44, 45], which corresponds to the value we have previously used in our numerical simulations and for calibration of our LII measurements.

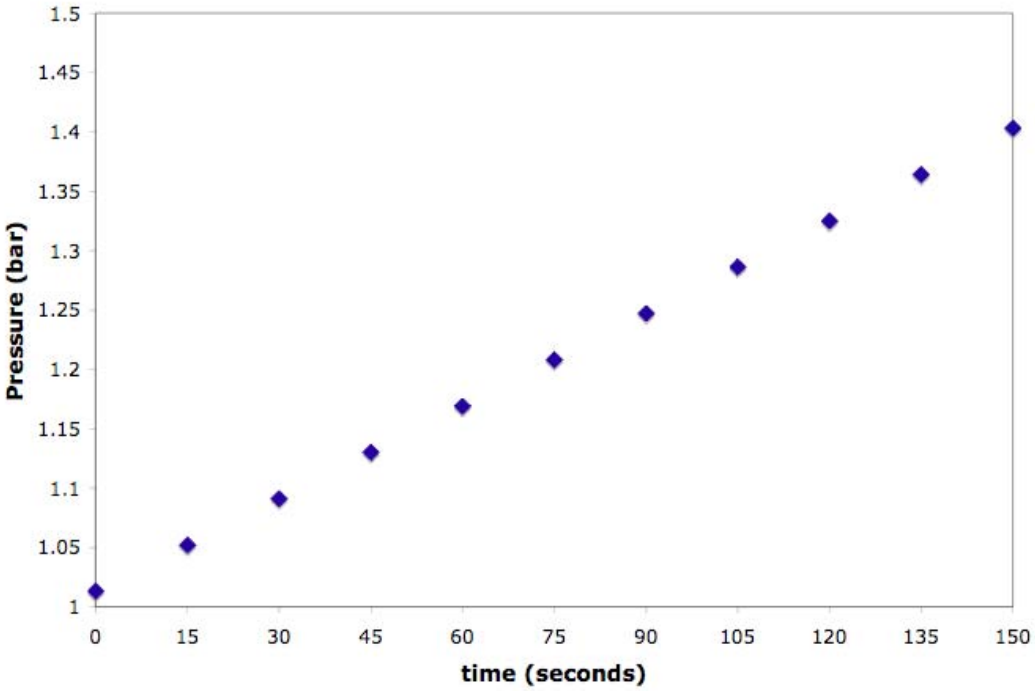

Fig. C1. Measured ambient pressure in the sealed experimental chamber. Data points correspond to flame images shown in the following Figs. C2-C7.

The results of this series of experiments are shown in Figs. C2-C7. Figure C2 (C5) displays the intensity of the green channel for the 70 cm/s (35 cm/s) flame. Figure C3 (C6) displays the temperature calculated using the two-color method, averaged from the three two-color combinations available for the 70 cm/s (35 cm/s) flame. Figure C4 (C7) displays the calculated soot volume fractions for the 70 cm/s (35 cm/s) flame, which were calculated using the profiles in Fig. C2 (C5) and the computed temperatures in Fig. C3 (C6). All data are labeled with the time of image acquisition, which corresponds to the time that has elapsed after sealing the experimental chamber. The chamber pressure for each image can be determined from the plot in Fig. C1.

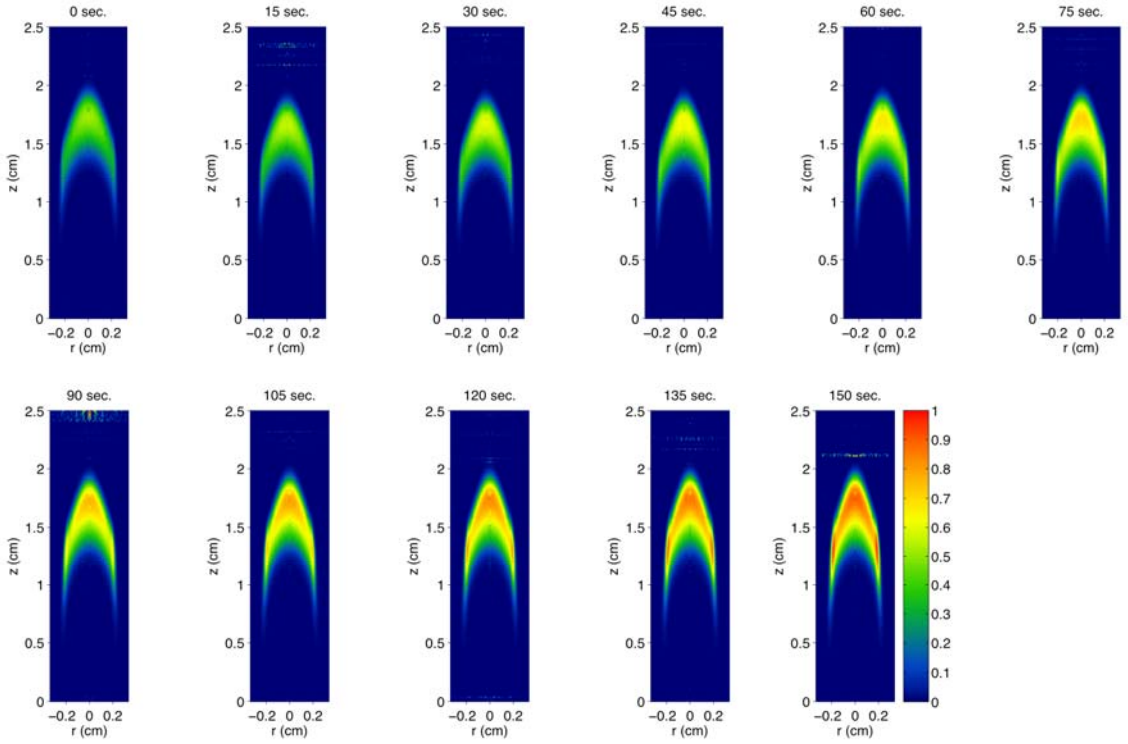

Fig. C2. Soot emission measured by the green channel of the camera for the 70 cm/s flame. The time after sealing the chamber is noted above each image.

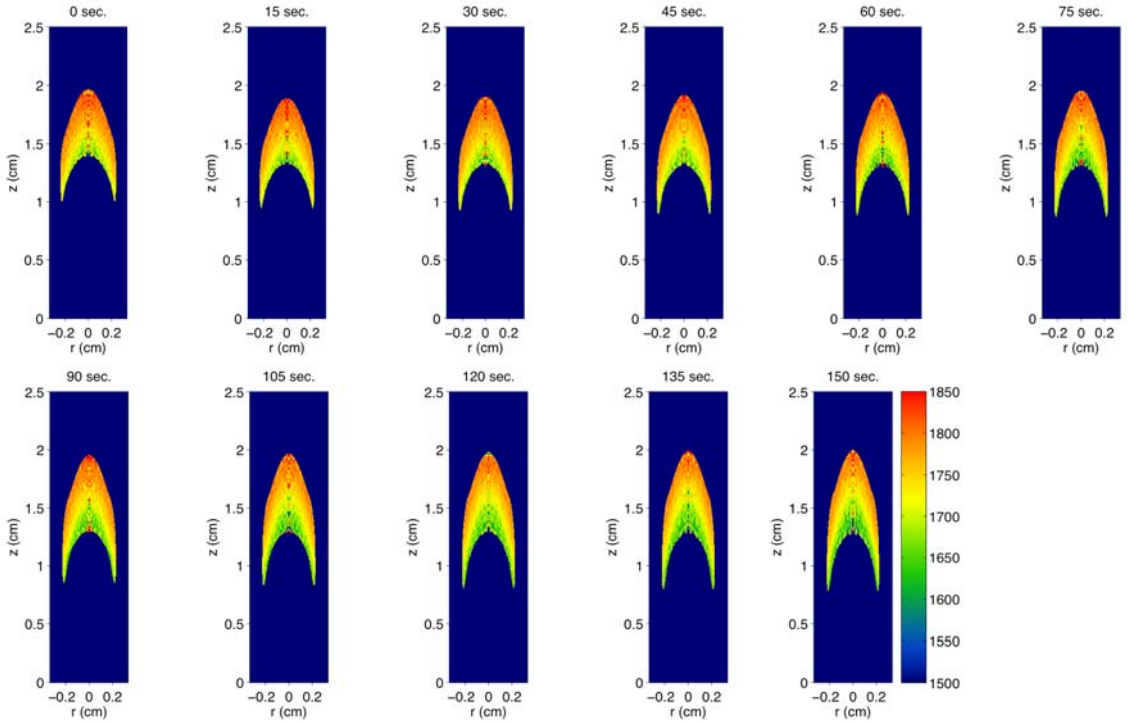

Fig. C3. Soot temperatures for the 70 cm/s flame. The time after sealing the chamber is noted above each image.

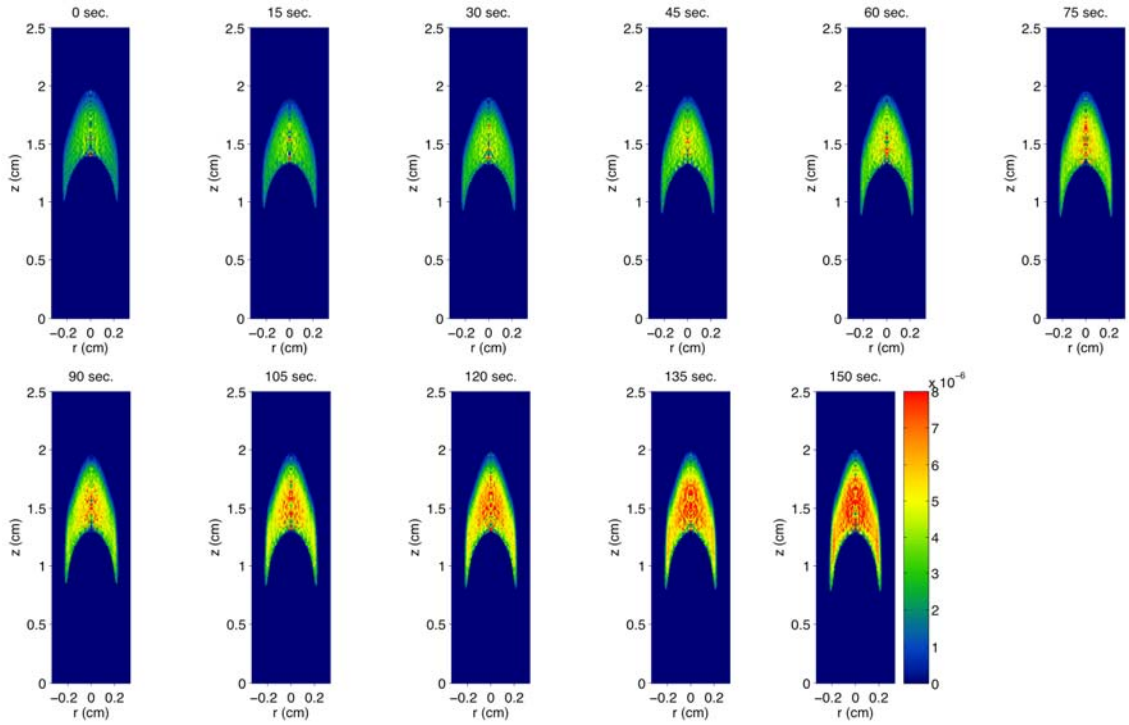

Fig. C4. Calculated soot volume fractions for the 70 cm/s flame. The time after sealing the chamber is noted above each image.

It can be seen in Fig. C2 that the intensity of soot emission from the 70 cm/s flame increases by about a factor of 2 over a run time of 150 seconds, which corresponds to an increase in pressure of 0.39 bar. It should also be noted that areas of highest intensity begin to migrate from the centerline towards the wings as the chamber is pressurized. Conversely, variations in temperature over the same pressurization (shown in Fig. C3) are minimal, with temperatures only in the lower area of the sooting region decreasing slightly. As a result, the overall soot volume fraction (shown in Fig. C4) is observed to double over the pressure range, as the location of peak soot also begins to migrate towards the wings. After 150 seconds, the maximum value of the soot volume fraction on the wings is comparable to the maximum value along the centerline at around 8 ppm.

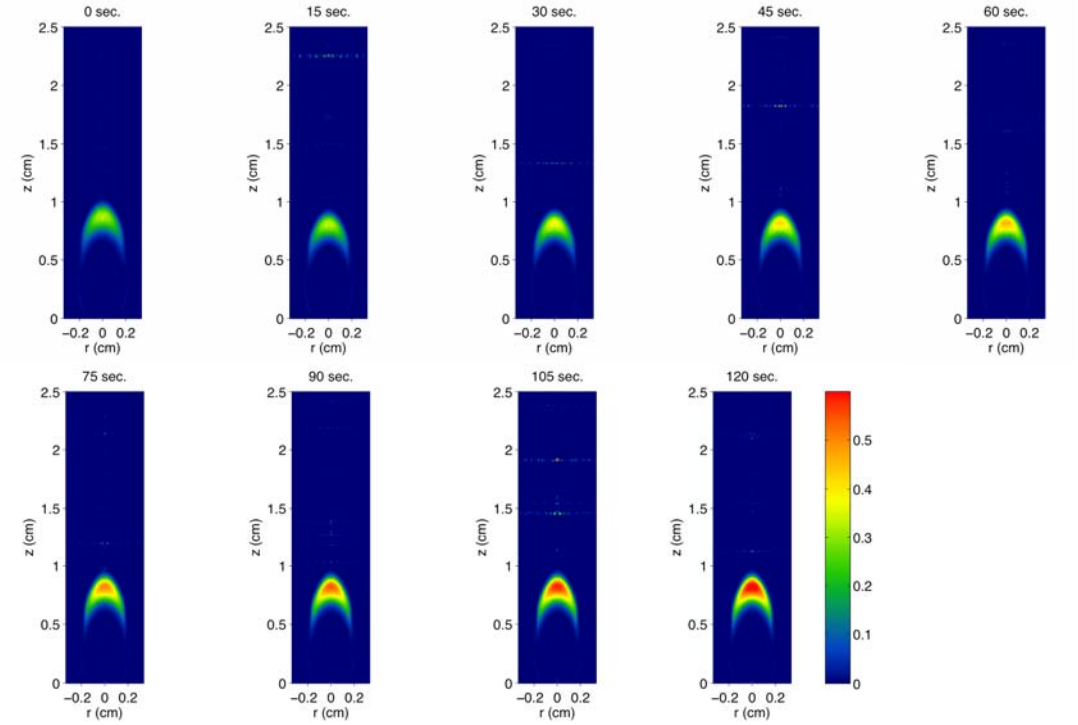

Fig. C5. Soot emission measured by the green channel of the camera for the 35 cm/s flame. The time after sealing the chamber is noted above each image.

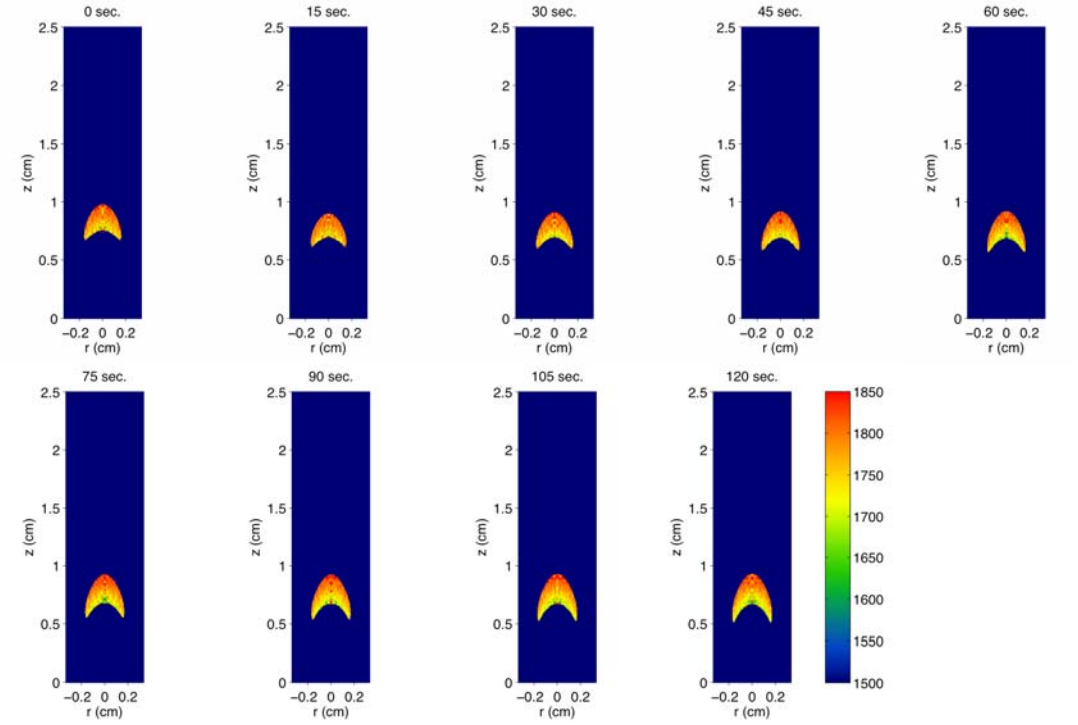

Fig. C6. Soot temperatures for the 35 cm/s flame. The time after sealing the chamber is noted above each image.

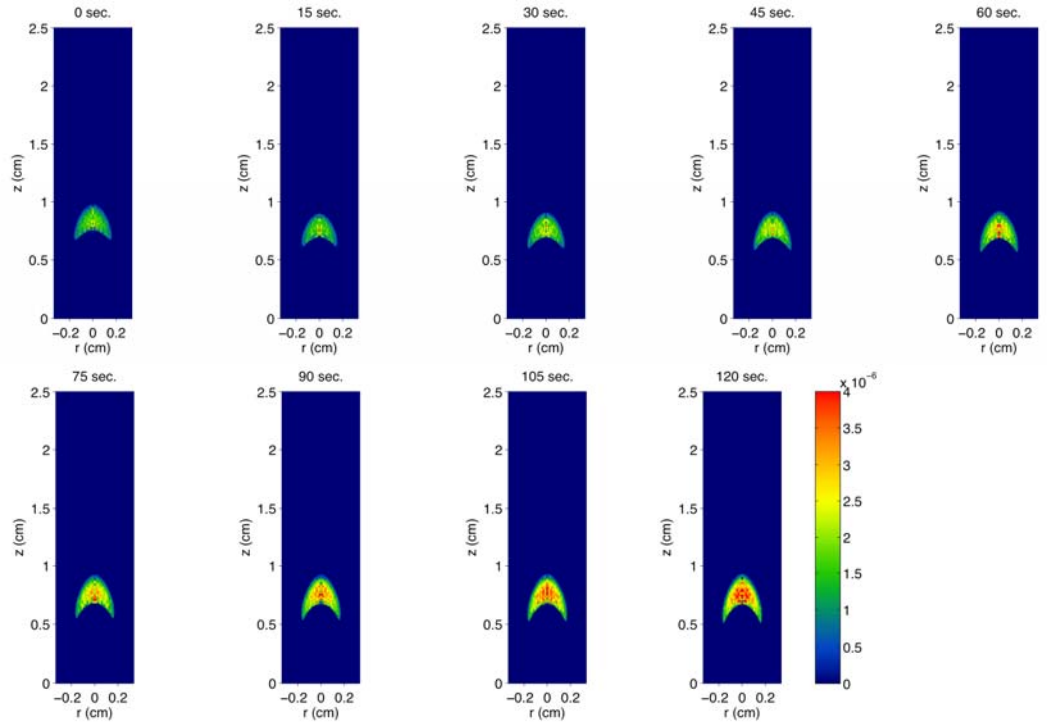

Fig. C7. Calculated soot volume fractions for the 35 cm/s flame. The time after sealing the chamber is noted above each image.

Similar to the 70 cm/s flame, the intensity of soot emission from the 35 cm/s flame (Fig. C5) increases by about a factor of 2 over a run of 120 seconds, which corresponds to an increase in pressure of 0.31 bar. Overall, the emission of the 35 cm/s flame is about 60% less intense than that of the 70 cm/s flame. The soot temperatures of the 35 cm/s flame (Fig. C6) are approximately 25 K higher than the temperatures of the 70 cm/s flame overall, and display minimal variations with the pressurization. The soot volume fractions of the 35 cm/s flame (Fig. C7) are approximately half that of the 70 cm/s flame, and are seen to increase by almost a factor of 2 over the pressure range.